



Royal Netherlands
Meteorological Institute
*Ministry of Infrastructure and the
Environment*

The spatial and temporal variability of the vertical dimension of rainstorms and their relation with precipitation intensity

Kenny Aberson

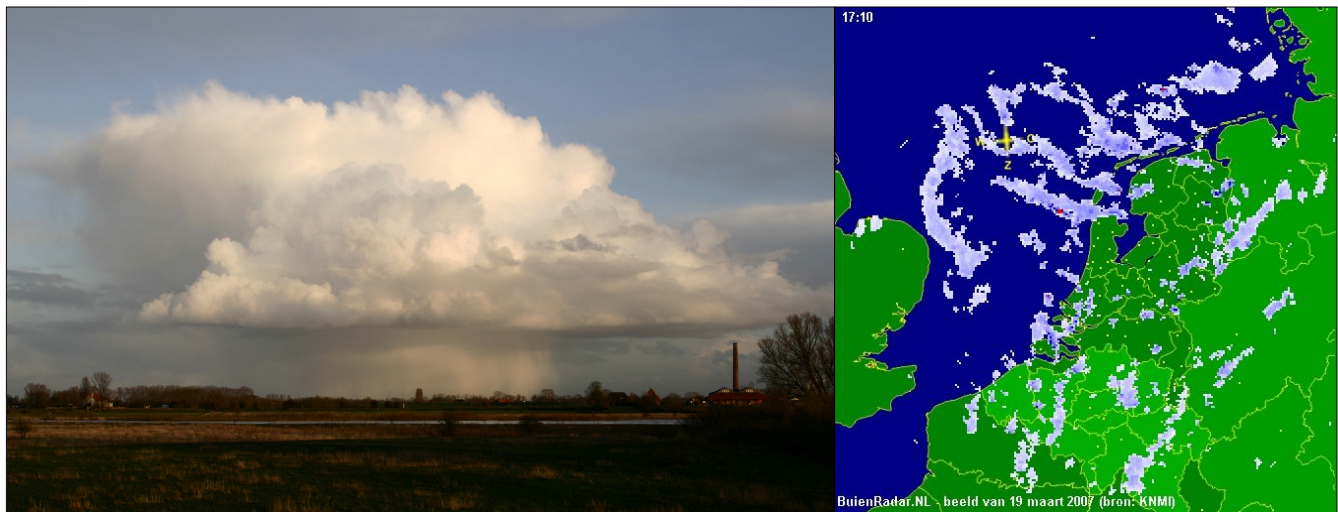
De Bilt, 2011 | Intern rapport; IR 2011-03

The spatial and temporal variability of the
vertical dimension of rainstorms and their
relation with precipitation intensity

Versie 1.0

Datum 28 oktober 2011
Status Definitief

The spatial and temporal variability of the vertical dimension of rainstorms and their relation with precipitation intensity



Kenny Aberson
October 2011
HWM-70424
Supervisors: A. Overeem (KNMI)
H. Leijnse (KNMI)
R. Uijlenhoet (WUR)

Abstract

Operational weather radar data are increasingly used for water management and climatological purposes, thanks to their high spatial and temporal resolution. The dimensions and timing are important factors determining the intensity of a rainstorm. This study presents an exploration of the spatial and temporal variability of the vertical dimension of rainstorms and their associated rainfall intensity. A measure for the vertical dimension of rainstorms is the echo top height (ETH), which is the maximum height of a precipitation echo. For this purpose, KNMI weather radar data were available for the period 2003-2010.

The spatial and temporal variability of ETH appears to be low over the Netherlands. Only during summer, the analysis shows higher average ETHs over the southwest and southeast, possibly related to the highest average temperatures observed. Moreover, a signal for a diurnal cycle of ETH is present for the summer period. However, the results are seriously affected by radar artefacts, due to (ground)clutter, beam filling, cloud overshooting and the limited number of elevation scans.

The spatial and temporal correlation between ETH and rainfall intensity in general is weak. Only for purely convective events there is some indication that ETH relates to rainfall intensity. This is supported by a case study conducted for the period June-August 2010. Possible explanations are radar artefacts, the nature of precipitation systems, the vertical profile of reflectivity and the geometry of a rainstorm.

Although the results of this study seem to be seriously affected by radar artefacts, the resulting report presents a unique multi-year, high resolution analysis of the spatial and temporal variability of ETH and its relation with precipitation intensity. Moreover, the evaluation of error sources affecting the analysis, produced a wealth of information that is relevant to the use of the operational ETH product. Finally, some recommendations are given in order to perform a more in-depth, quantitative study.

Table of Contents

| | |
|---|----|
| 1. Introduction..... | 4 |
| 2. Background..... | 5 |
| 2.1 Radar basics..... | 5 |
| 2.1.1 Precipitation intensity product..... | 5 |
| 2.1.2 ETH product..... | 6 |
| 2.2 Error Sources..... | 7 |
| 2.3 The vertical dimension of rainstorms..... | 10 |
| 3. Data & Method..... | 11 |
| 3.1 Data..... | 11 |
| 3.2 Spatial and temporal variability of ETH..... | 11 |
| 3.3 Relation between the ETH and precipitation intensity..... | 13 |
| 4. Results – Spatial and temporal variability of ETH..... | 15 |
| 4.1 Average ETH 2003-2008..... | 15 |
| 4.2 Diurnal Cycle ETH 2003-2008..... | 21 |
| 5. Results - Relation between ETH and precipitation intensity..... | 25 |
| 5.1 Spatial and temporal correlation..... | 25 |
| 5.2 Case study summer 2010..... | 26 |
| 6. Discussion..... | 30 |
| 6.1 Spatial and temporal variability of ETH..... | 30 |
| 6.2 Implications for the operational use of the ETH product..... | 32 |
| 6.3 Relation between the ETH and precipitation intensity of storms..... | 33 |
| 7. Conclusion and recommendations..... | 34 |
| References..... | 37 |

1. Introduction

Rain intensity radar data is, besides operational use, increasingly used for hydrologic and climatologic purposes. Radar data is now applied in calculating extreme rainfall statistics for the use and the design of hydraulic systems (Overeem et al., 2009a). These purposes require high temporal and spatial resolution data, which is offered by radar data rather than traditional rain gauges. Usually damage resulting from extreme rainfall involves high costs. Moreover, extreme rainfall events are expected to increase due to climate change. The weather radar offers the possibility to calculate accurate extreme rainfall statistics as well as derivation of the vertical and horizontal dimensions of rainstorms. The dimensions of rainstorms are closely related to the rainfall produced by a rainstorm (Gagin et al., 1984; Adler and Mack, 1984; DeMott and Rutledge, 1997). The focus of this study is on the vertical dimension of rainstorms.

The vertical dimension of rainstorms influence the spatial and temporal distribution of rainfall. The vertical dimension, or cloud top height, is a measure of updraft strength and therefore severity of storms (Delobbe and Holleman, 2006). During summer, intense thunderstorms often have a large vertical extent and can easily reach over 10 km of height. Moreover, it gives insight into the three-dimensional structure of convective cells as well as frontal, stratiform precipitating systems (Wessels, 2006). Information about cloud top height is also relevant to aviation. From a climate modeling point of view, (mathematical) relations between the dimensions of precipitation systems can be useful for parameterization of processes.

This report presents an exploration of seasonal, diurnal and regional dependencies of the vertical dimension of rainstorms. The so-called Echo top height (ETH) has been chosen as a measure of the vertical dimension of a rainstorm. The ETH is defined by the maximum height of a precipitation echo detected by the weather radar. High resolution ETH and precipitation intensity data were available for the period 2003-2010 for the Netherlands. ETH radar data is used operationally by weather institutes and companies. Nevertheless, it has not yet been used to explore multi-year spatial and temporal variability of rainstorm height over the Netherlands. Further, the ETH will be related to precipitation intensity.

The aim of this study is condensed in the following research questions:

- Does the ETH show any spatial or temporal variability over the Netherlands for the period 2003-2008?
- What is the relation between precipitation intensity and the ETH of rainstorms?

The remainder of this report starts with a short background (Chapter 2) on radar basics and error sources affecting the quality of ETH radar data. Chapter 3 describes the data and method used for the analysis. Moreover, two corrections on the radar data are evaluated. The results are presented in Chapters 4 and 5. Chapter 4 focuses on the vertical dimension of rainstorms, while Chapter 5 presents the results of the relation between the ETH and the precipitation intensity. This report ends with a discussion (Chapter 6) and conclusion and some recommendations (Chapter 7) towards a more in-depth, quantitative study of the dimensions of rainstorms.

2. Background

2.1 Radar basics

A weather radar transmits electromagnetic pulses which are reflected by hydrometeors and visualized as radar images by a central computer system. The KNMI radars (located in Den Helder and De Bilt) transmit pulses with a repetition frequency of 250 Hz and a peak power of approximately 260 kW. The transmitted electromagnetic energy is not distributed along a straight line but has a particular shape, the so-called antenna beam pattern. This shape is approximately Gaussian with a main lobe of peak power in the center of the antenna and side-lobes of relatively high power at approximately 2° from the axis of the beam. The effective width of the radar beam is defined as the beamwidth. The beamwidth is the width (in degrees) of the antenna beam where the power is at least half of the maximum power of the main lobe (Rinehart, 2006). The beamwidth of the KNMI radars is 1.0° . It is an important parameter determining the scanning volume of the radar. Radars rotate along a vertical axis and are capable of scanning both horizontally as well as vertically. The horizontal range is 120-320 km, depending on the elevation scan. The detection and processing of the precipitation intensity and ETH product is done by using different methods, which will be discussed next.

2.1.1 Precipitation intensity product

For the detection and derivation of the location and intensity of rainfall for the period 2003-2007 the following procedure is applied. For radar reflectivity data of rain intensity vertical elevation scans at 0.3° , 1.1° , 2.0° and 3.0° are interpolated to produce pseudo-CAPPI radar images (Wessels, 2006) at 800 m height at a range of 15-80 km from the radar. Since 2008, this height is 1500 m. The volume coverage pattern (VCP) for precipitation intensity, resulting from the scanning geometry of the radar, is depicted in Fig. 2.1 (Overeem et al., 2009b).

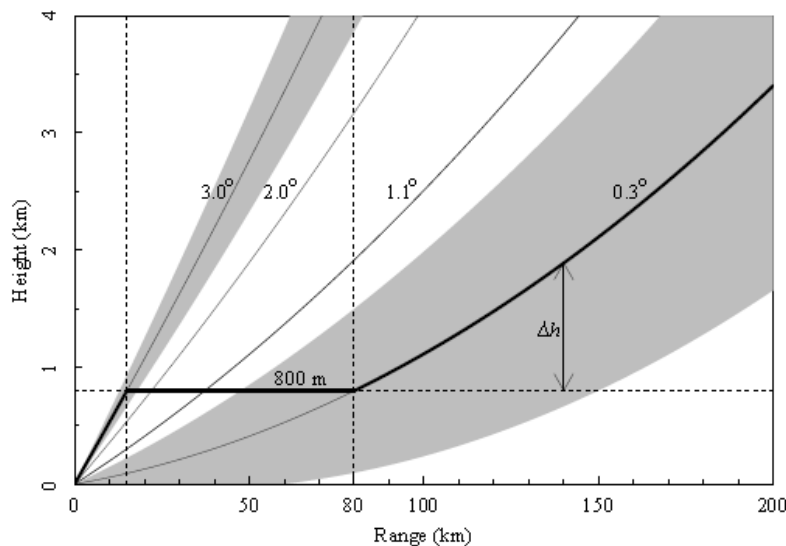


Figure 2.1 Volume coverage pattern of the KNMI radars, used for the production of the precipitation intensity product used for the period 2003-2007. The thick line displays the pseudo-CAPPI image. Thin lines denote the center of the radar beams, while the grey shaded area represents the beamwidth of the radar beam. (Overeem et al., 2009b)

The lowest elevation beam is used for the range 80-200 km from the radar. Close to the radar, the 3° beam is used to detect precipitation echoes.

To convert the received reflected power by the antenna to rain intensity, the radar equation is applied (Eq. 2.1) and the equation for the Z-R Relationship (Eq. 2.2). The radar equation relates the received reflected power P_r to the radar reflectivity factor z . A derivation can be found in Rinehart (2006).

$$P_r = \frac{\pi^3 P_t G^2 \varphi \theta c t |K|^2 l}{1024 \ln(2) \lambda^2 r^2} z \quad (2.1)$$

Where P_t is the transmitted peak power, G is the gain of the antenna, φ is the vertical beamwidth, θ is the horizontal beamwidth, c is the speed of light, t refers to the time between transmitted and received wave, K is a constant depending on the material, temperature and the wavelength of the radar, l being the attenuation term, λ is the wavelength, r is distance from the radar and z refers to the radar reflectivity factor.

This equation yields the radar reflectivity factor z ($\text{mm}^6 \text{ m}^3$), denoted as Z (dBZ) on a logarithmic scale. Finally, the Z-R relationship converts the radar reflectivity factor into precipitation intensity R (mm h^{-1}). The most common one (Marshall et al., 1955, Eq. 2.2) is used by the KNMI.

$$Z = 200 R^{1.6} \quad (2.2)$$

2.1.2 ETH product

For the ETH, a different procedure is followed. The ETH is the maximum height (in km) where an echo of at least 7 dBZ ($\approx 0.1 \text{ mm/h}$) is measured. Usage of pseudo-CAPPI images is not useful in this case, since interpolation to the 800 m altitude would severely underestimate ETHs. For the derivation of ETH all elevations scans have to be used. The scanning scheme for the ETH product consists of 14 elevations. The resulting VCP is depicted in Fig. 2.2. The elevations are in the range of $0.3^\circ - 12.0^\circ$, but do sometimes slightly differ from the elevations depicted in Fig. 2.2. Objects detected within the beamwidth of a certain elevation beam will be assigned to the center of that particular beam. For instance, Fig. 2.2 shows that an object detected at a range of 100 km at 1.3 km will be assigned to the center of the lowest beam and consequently have the value of 1.5 km.

For the processing of the ETH product the radar equation (Eq. 2.1) is applied to derive the radar reflectivity that corresponds to the received reflected power by the radar antenna. Finally, the maximum height is determined at which a precipitation echo of at least 7 dBZ is measured. In 2008, the operational radars in Den Helder and De Bilt were upgraded. The most important features being the higher spatial and temporal resolution and different scanning elevations. This affects both the precipitation intensity as well as the ETH product. The different scanning geometry influences the ETH product most and is discussed shortly here. Since 2008, the elevation ranges from 0.3° to 25° (Beekhuis and Holleman, 2010). A low elevation scan of 0.4° was added to decrease errors related to large volumes at farther distances. Scans of 25° , 20° and 15° were introduced to detect high ETHs close to the radar. The total number of elevations has not been changed.

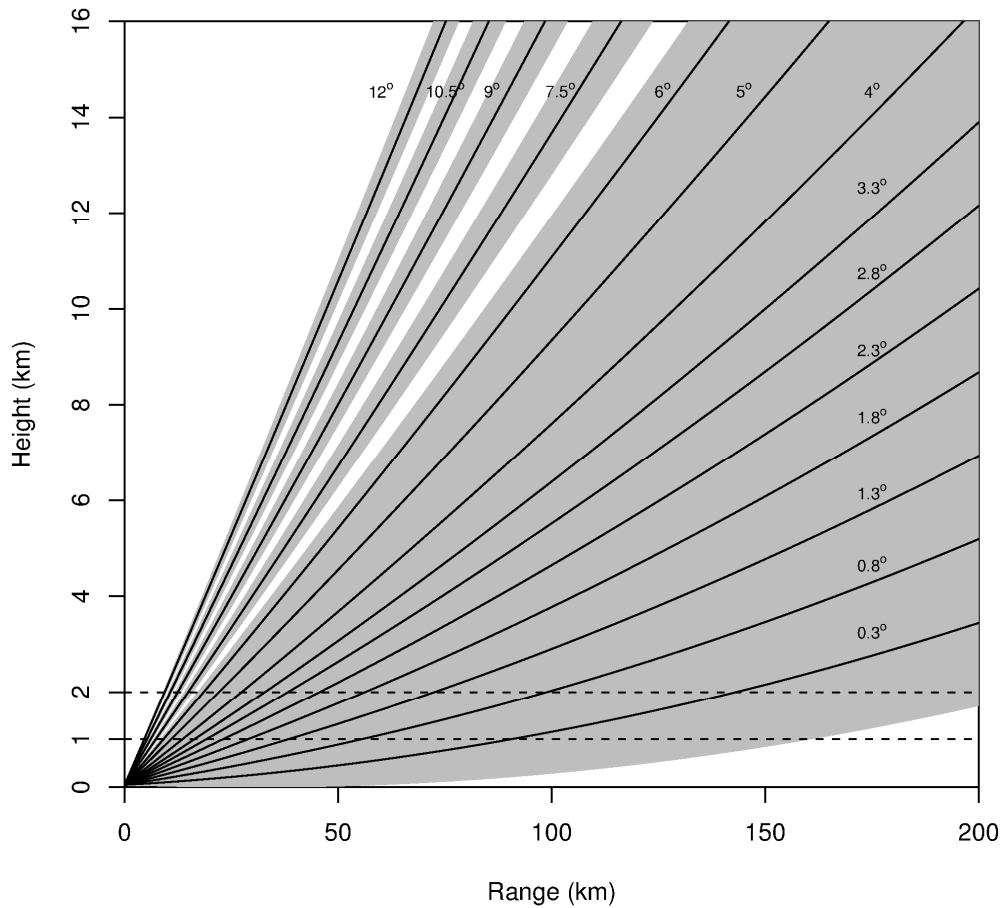


Figure 2.2 Volume coverage pattern of the KNMI radars used for producing the ETH product. It displays the height of the antenna beam as a function of the range from the radar. Thick lines denote the center of the different elevations (0.3° – 12.0°) of the radar beams. The grey shaded areas represent the beam width (1°) of the antenna beams.

2.2 Error Sources

Several sources of errors affect the quality of the radar rainfall intensity and ETH data sets. Michelson et al. (2005) give a comprehensive overview. This report will only treat the most relevant error sources for this study. The most important sources of errors with respect to precipitation intensity are (a) ground clutter, (b) the vertical profile of reflectivity (VPR), (c) the drop-size distribution ($Z-R$ relationship) and (d) attenuation of reflectivity by heavy precipitation (Holleman, 2006, Overeem et al., 2009a).

Ground Clutter is the detection of non-hydrometeors by the main radar beam and side-lobes crossing the ground. Ground Clutter is usually most severe close to the radar and comprises echoes related to buildings, trees and other non-hydrometeors. Ground clutter is corrected operationally by the radar computer.

The vertical profile of reflectivity (VPR) refers to the vertical dependence of reflected precipitation echoes. Precipitation intensity usually shows a vertical profile. The shape of the profile depends on the type of precipitation. Overeem et al. (2009b) shows a VPR exists, based on comparison

of radar reflectivity data with data from rain gauges. A positive or negative VPR gradient exists for respectively summer (convective precipitation) and winter season (stratiform precipitation). This effect can cause underestimation or overestimation of precipitation intensity, depending on the height at which the precipitation echo is measured and the shape of the VPR. For instance in summer, stronger precipitation cores sometimes exist aloft, causing overestimation of precipitation intensity. Corrections include adjustment to rain gauges as well as interpolation by the use of pseudo-CAPPI images.

The drop-size distribution determines the relation between the measured reflectivity and the precipitation intensity. This is an empirical relation validated by drop-size observations by Wessels (1972). From this validation, it became clear that for individual rainfall events deviations from Eq. 2.2 can be large. This is largely due to the radar reflectivity factor Z being proportional to the sixth power of the diameter of a hydrometeor (Rinehart, 2006).

Attenuation of reflectivity by severe precipitation occurs when heavy precipitation diminishes the energy of the radar beam to such an extent that precipitation at farther distances from the radar cannot be measured anymore. July 17 of 2004 as well as June 28 of 2011 are striking examples of severe attenuation of reflectivity. The precipitation intensity radar data have already been corrected by comparison with data from rain gauges for various error sources, such as ground clutter and the VPR gradient by the work of Overeem et al. (2009b)

Error sources that affect the quality of the ETH product are (a) (ground) clutter, (b) overestimation due to side-lobes, (c) errors due to the limited amount of elevation scans, (d) errors at large range from the radar due to the curvature of the earth (overshooting) and the increase of the scanning volume, (e) errors due to the “cone-of-silence” and (f) errors due to incorrect correction for refraction (Wessels, 2006; Maddox et al., 1999, NASA, 1997; Takacs et al., 2004).

Ground clutter has already been discussed for precipitation intensity. Ground clutter for the ETH data set has been corrected for this study by using the precipitation intensity data set, which has already been corrected by Overeem et al. (2009a). Moreover, the detection threshold of 7 dBZ is quite low and might cause detection of spurious ETHs. These can originate from planes or reflections from the tropopause. An example is given in Fig. 2.3.

Unrealistic high ETHs also originate from overestimation of ETH due to side-lobes. The main radar beam might be significantly higher than the cloud top of a storm, while the lower side-lobe might still detect an echo from the cloud top. Especially at increasing distance from the radar station, the errors due to side-lobes might lead to strongly overestimated ETHs. A side-lobe correction is applied operationally by the KNMI. Correction for (ground) clutter will be elaborated in Chapter 3.

Underestimation or overestimation of ETH due to the detection and interpolation problems can be attributed to the limited amount of elevation scans. This error source can be clarified by the volume coverage pattern of the ETH product (Fig 2.2). The amount of elevation scans is limited, leading to gaps in the detection of ETH for elevation scans in the range of 6° to 12° . This can cause a typical ring-shaped gradient of the ETH (Fig. 2.4).

From the VCP for the ETH product (Fig. 2.2) follows that the lowest detectable ETH becomes gradually higher at farther distances from the radar station. The lowest (0.3°) radar beam might overshoot a rainstorm at far distance from the radar. As the scanning volume increases strongly with distance (Fig. 2.2), the edge of the lowest main beam might still detect an echo. This echo will be attributed to the main beam, thereby overestimating the actual storm top. This effect might very well be present over the Netherlands as the areas near the border are located at more than 150 km from the least distant radar. Thus, at large distances the large beamwidth and large distances between the lowest beams can cause large errors.

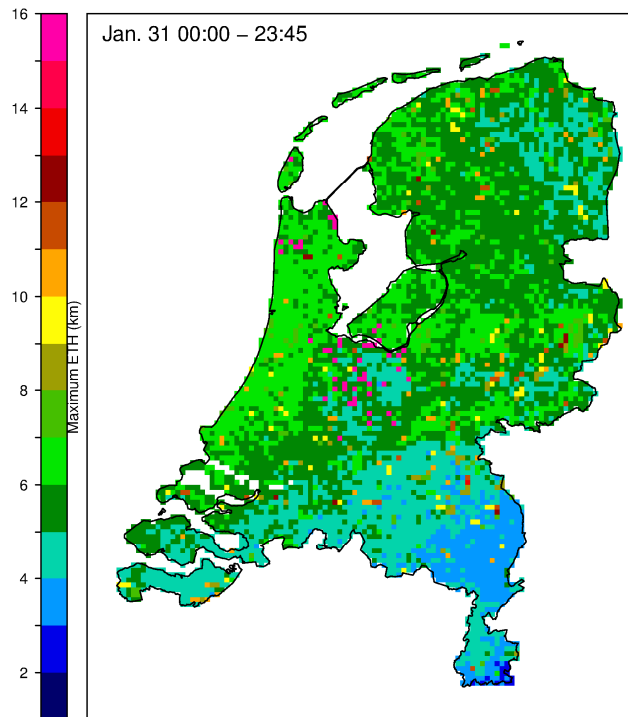


Figure 2.3 Maximum ETH over a 24-hour period (31-01-2004). Yellow/Orange and reddish pixels correspond to ETHs higher than 9 km, which hardly occur during winter. In addition, they are much higher than the surrounding pixels.

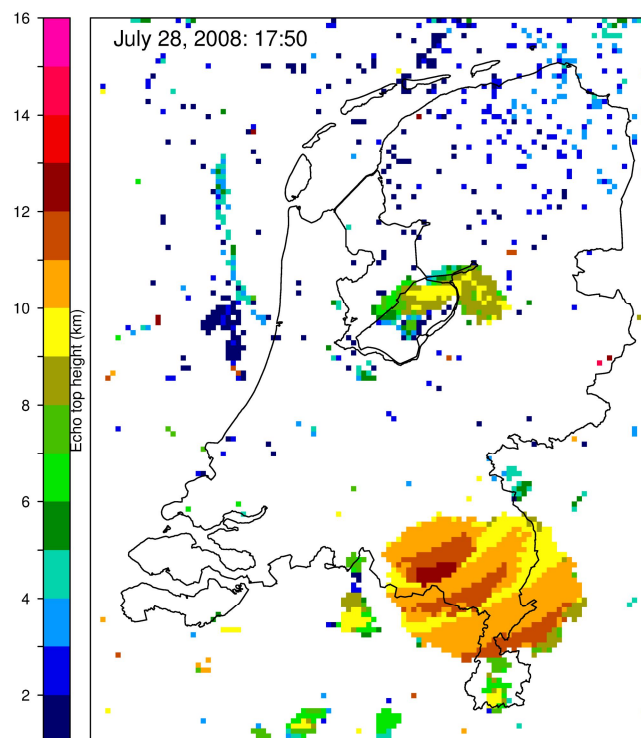


Figure 2.4 Typical ring-shaped gradients of ETH detected in a severe thunderstorm (28-07-2008: 17.50 UTC). Note that the height differences between the successive rings are exaggerated due to the color scale.

Moreover, a typical feature called “the cone-of-silence” can be derived from the VCP. At near distance from the radar, the highest elevation scan (12°) cannot detect high ETHs. At 25 km distance, the radar is not able to detect ETHs higher than 5 km. This can lead to underestimation of ETH. The latter two sources of errors are described in more detail by Wessels (2006), DeLobbe and Holleman (2006) and Maddox et al. (1999). Several corrections are suggested, the most convenient for this study being the use of a radar composite from both the Den Helder as well as the De Bilt radar images. The radar composite is processed as follows. For distances larger than 150 km, the ETH of the nearest radar is chosen. The highest tops are selected within 150 km from any radar. This is most probably equivalent to disregarding the nearest radar.

Finally, errors due to superrefraction and subrefraction by the atmosphere can overestimate (superrefraction) or underestimate (subrefraction) ETH. This can lead to errors up to 1.2 km height (NASA, 1997). KNMI uses a normal refraction coefficient which is only valid for average conditions and objects below 10 km (Wessels, 2006). Information from soundings can predict whether superrefraction or subrefraction occurs. However, this is elaborate and for this study the normal refraction coefficient is used.

2.3 The vertical dimension of rainstorms

The cloud top height is the level at which the cloud is not able to grow further anymore in the vertical. The tropopause is an important limiting factor for the ultimate cloud top height. At the tropopause a strong temperature inversion prohibits further vertical development of clouds. The height of the tropopause varies in time and location. The mean tropopause height during winter is considerably lower than during summer.

The updraft strength determines whether the potential cloud top height will be reached. The updraft strength is a measure for the buoyancy, which in turn is determined by the thermodynamical stability of the atmosphere. Large-scale vertical motions and vorticity can force air to move in the vertical, thereby contributing to updraft strength

The height of the tropopause and updraft strength vary in time. In winter the height of the tropopause is relatively low and updraft strength is generally weak. Resulting cloud top heights will be relatively low. During summer, the height of the tropopause can become higher than 10 km and updraft strength can be vigorous due to large thermodynamic instability. Cloud top height can reach up to 15 km during summer.

Different cloud types have distinct cloud tops. Several precipitating cloud types exist. Among the precipitation clouds, nimbostratus and cumulonimbus are usually associated with the highest precipitation amounts. Nimbostratus is usually associated with low-level clouds accompanying frontal zones. Cumulonimbi are frequently observed during summer, giving rise to intense precipitation. The winter is dominated by stratiform precipitation by frontal zones having moderate to high tops, but low precipitation intensity. Convection is usually shallow with moderate to high precipitation intensity. During summer, deep convection with very high cloud tops are often associated by intense precipitation. Stratiform precipitation occurs as well and is not seldom accompanied by embedded convection. Mesoscale convective systems developing from single thunderstorms have very high tops with distinct areas of both high precipitation as well as low intensity stratiform precipitation.

3. Data & Method

3.1 Data

For this study precipitation intensity and ETH data sets measured by the De Bilt and the Den Helder radars for the period May 2003 - December 2008 were available. The spatial and temporal resolution of both data sets is respectively 2.5-km and 15-min. The 2003-2008 data set is used for the multi-year analysis of the spatial and temporal variability of ETH and the relation with precipitation intensity. Higher resolution (1 km, 5 min) data is available for 2009-2010. A subset of the data set of 2010, containing only convective rainfall events, is used to study the relation between ETH and precipitation intensity in more detail. Only 2 years (2009 and 2010) of these high resolution data were available, which makes this set unsuitable for multi-year analysis of ETH. The 2003-2008 and 2009-2010 data sets have different spatial and temporal resolutions and a different scanning geometry (Section 2.1). Thus, the 2009-2010 data set could not be combined with the 2003-2008 data set.

The average annual data availability for 2003-2008 is higher than 82%, ranging from 59% (2003) to 91% (2008). Only the data availability for July 2003 (24%), September 2003 (33%), December 2003 (4%) and January 2004 (44%) is low. The data availability is defined as the availability of all pixels of both precipitation intensity and ETH data for a certain time. Thus, on average all pixels of both data sets are available 82 out of 100 times. For the case study conducted for the summer of 2010, the data availability is 99.2% (June), 98.8% (July) and 99.2% (August).

In this study two analyses are performed. The first is the exploration of the spatial and temporal variability of ETH. The second is the relation between ETH and precipitation intensity. Next, the methods of both analyses are discussed in more detail.

3.2 Spatial and temporal variability of ETH

To explore the spatial and temporal variability of ETH both precipitation intensity as well as ETH data sets are used. First, the data sets have to be corrected for the error sources discussed in Chapter 2.

The precipitation intensity data set has been corrected indirectly for several error sources, such as clutter and the VPR by validation with data from rain gauges (Overeem et al., 2009b). For the purpose of this study, two algorithms have been implemented to correct the ETH data set for (ground) clutter. These are (a) a precipitation filter and (b) a 3x3-pixels median filter.

Firstly, clutter is removed by linking the ETH data set to the clutter-corrected precipitation intensity data set: a so-called precipitation filter. Overeem et al. (2009b) present a method to correct precipitation intensity radar images for several error sources, such as clutter. They used data from rain-gauge networks to adjust radar-based precipitation accumulations. Next, ETH pixels that do not correspond to a precipitation pixel are discarded. This will reduce the amount of clutter in the ETH data set. However, applying a precipitation filter does still not completely remove anomalous ground clutter. Fig 3.1 shows the average monthly amount of radar images, equivalent to the number of 15-min time steps, on which an ETH was detected. Application of a precipitation filter reduces the large amount of ground clutter occurring close to the radar, which gives rise to unrealistic low ETHs.

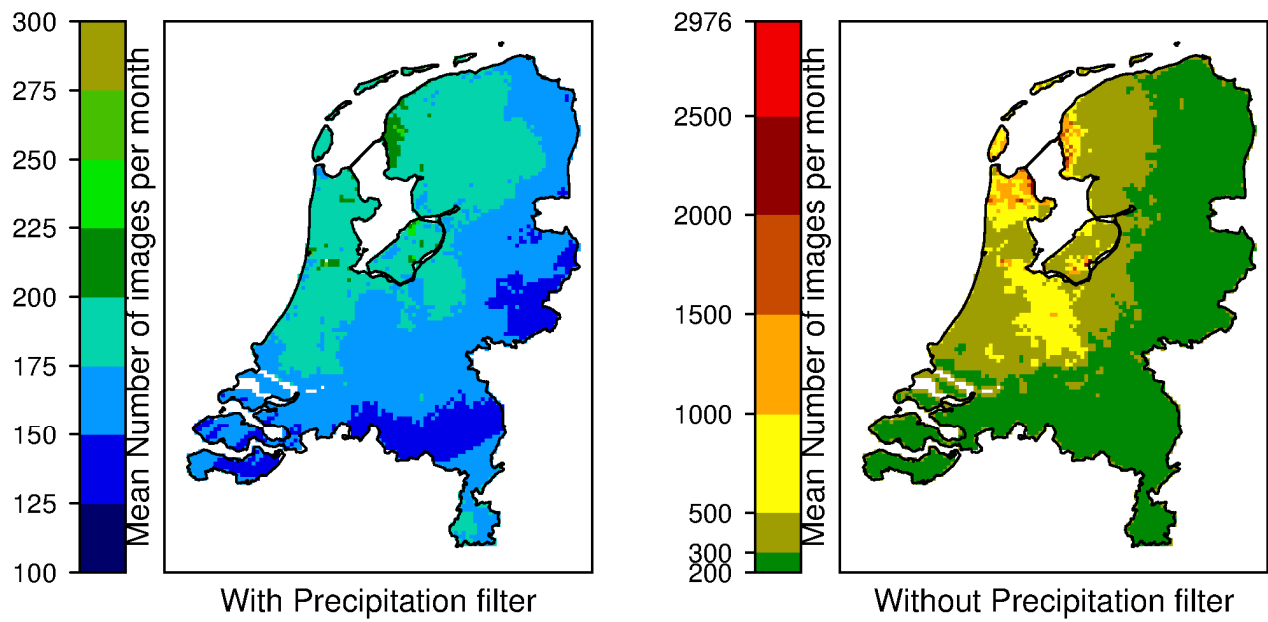


Figure 3.1 Mean number of ETH images per month, with and without the application of a precipitation filter. Monthly averages are based on the year 2008, which has a large spatial variability in ETH.

Moreover, for locations at farther distance from the radar the number of ETH radar images is higher when the precipitation filter is not applied, in comparison with application of the precipitation filter. This is an indication that ground clutter and echoes related to detection of non-hydrometeors such as birds, insects, planes and reflections by the tropopause is also removed by the precipitation filter. The precipitation filter has been applied on all analyses of the spatial and temporal variability of ETH. The effect of the application of the precipitation filter on the average ETH for the year 2008 has been quantified. The average ETH with precipitation filter is subtracted by the average ETH without precipitation filter.

The impact of the precipitation filter on mean ETH is an increase up to 3 km. This implicates that ETH clutter is characterized by low values. The areas showing an increase in ETH appear to be similar to the areas where clutter is detected (Fig. 3.2). For locations located at greater distance from the radars the increase is in the order of 0 to 0.5 km.

Secondly, a 3x3 pixel median filter is applied to remove spurious ETH pixels that do correspond to precipitation pixels. These spurious pixels, having relatively high ETH values, originate from side-lobe errors, superrefraction, incorrect elevation readings and other noise due to the very low level of detection (7 dBZ). The 3x3 pixel median filter evaluates for every single cell the median of the 8 neighboring pixels and center pixel. Subsequently, the single cell will be given the value of this median. This will remove the high spurious ETH pixels abundantly present in the ETH data set (Fig. 2.3). The median filter has only been applied on analyses where spurious ETH pixels have large impact, such as the calculation of the maximum daily amplitude of ETH. It has not been used for analyses of the average ETH. Quantification of the effect of the median filter on the average ETH shows that it is hardly affected by using the median filter. Differences are in the order of 0.05 km. This is an indication that spurious ETHs do hardly affect the average ETH.

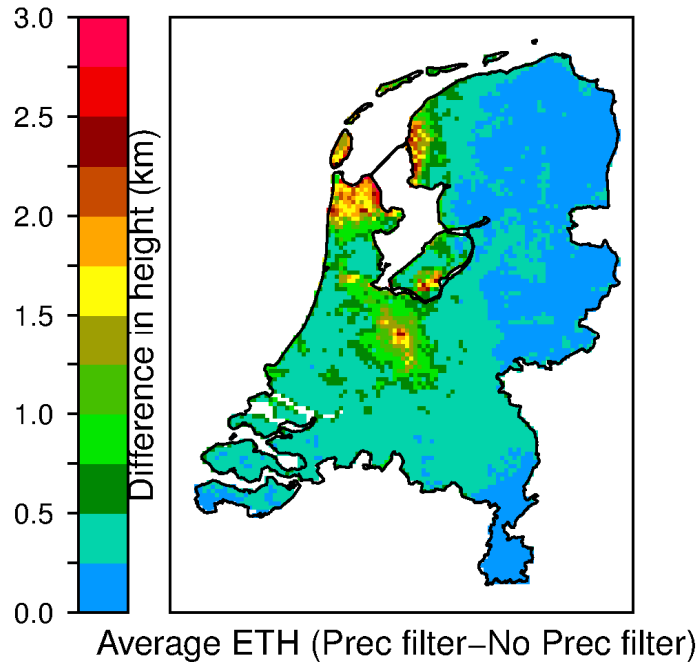


Figure 3.2 The difference in ETH (km) when the average ETH using the precipitation filter is subtracted by the average ETH without using the precipitation filter. Based on the year 2008, which shows spatial large variability in ETH.

After the two corrections have been applied, the spatial and temporal variability of ETH has been explored for the period 2003-2008. It should be stressed that this report has an exploratory nature. Some recommendations are given in Chapter 7 in order to perform a more in-depth, quantitative study.

3.3 Relation between the ETH and precipitation intensity

After correcting and analyzing the spatial and temporal variability of ETH for the period 2003-2008, the relation between ETH and precipitation intensity is assessed. For this purpose, the spatial squared correlation coefficient (R^2_{spatial}) as well as the temporal squared correlation coefficient (R^2_{temp}) between ETH and precipitation intensity are calculated. The calculation of R^2_{spatial} is based on the average and standard deviation of all pixels over the country for all seasons over the period 2003-2008. This yields one value for R^2 for every season, which is a measure for the instantaneous correlation in space between the average ETH and the total precipitation depth. R^2_{temp} is computed for every single pixel and yields the squared correlation coefficient over all time steps. Due to computational limitations, the temporal squared correlation coefficient could not be calculated for seasons over the full 6-year period. Therefore it is calculated for every month over the period 2003-2008.

Extreme precipitation is usually associated with high precipitation intensity concurring with severe convective precipitation events. For this purpose, data on the occurrence of convective clouds were available for the period June 2010 - August 2010. A weather forecaster has evaluated several data sources for 14 air bases and airports to recognize cumulonimbus clouds (CBs) every 30 minutes. These data sources include radar and satellite images, atmospheric stability data from radiosondes, analysis of synoptic systems on weather maps, visual observations of CBs (if available) and lightning detection

data. This has resulted in an extensive overview of the occurrence of CBs during the summer of 2010. Only CBs within a radius of 15 km from the particular air base or airport have been recognized. This implicates that the Netherlands is not completely covered (Fig. 3.2).



Figure 3.3 The 14 circles represent the areas in which a weather forecaster investigated the presence of CBs.

However, a large part of the country is covered by the observations, because of which most CBs will be detected. Exceptions include the detection gaps in the middle, northeastern and southwestern part of the country. Observations by the weather forecaster were done every 30 minutes, while the temporal resolution of the data sets for this study is 5 min. It is assumed that between two consecutive half-hourly observations of CB clouds, convective storms are present over the country. Finally, for the selected CB events the spatial and temporal correlation between ETH and precipitation intensity is calculated. Additionally, a cell recognition algorithm has been utilized to relate the ETH to the precipitation intensity of a storm cell for the period June – August 2010. The cell recognition algorithm (Wessels 2006, adapted from Gonzalez and Woods, 1992) recognizes cells of connected pixels and computes the number and size (km^2) of storm cells as well as precipitation characteristics, such as average and maximum intensity, per 5-min radar image. The recognition of storm cells is based on the precipitation intensity data set. By combining the recognized storm cells with the ETH data set, information can be gained about the ETH characteristics, such as average and maximum ETH, per storm cell. A threshold for the minimum size of a rainstorm (50 km^2) is used to exclude cells caused by clutter and noise. The threshold for precipitation intensity is set at 0.1 mm per 5 min.

4. Results – Spatial and temporal variability of ETH

4.1 Average ETH 2003-2008

The average seasonal ETH per pixel has been calculated to explore the spatial and temporal variability of the ETH of storms. In Fig. 4.1 the average ETH for the winter (DJF) and summer (JJA) season are depicted. The average ETH has been calculated over all 15-min radar images, except for non-existing and nodata-images. The median filter was not applied. The average ETH shows a clear gradient. The lowest values are found near the radars in De Bilt and Den Helder, while values appear to increase circularly farther from the radars. Average ETH for the summer period shows a distinct gradient as well, the average ETH being approximately 2 km higher.

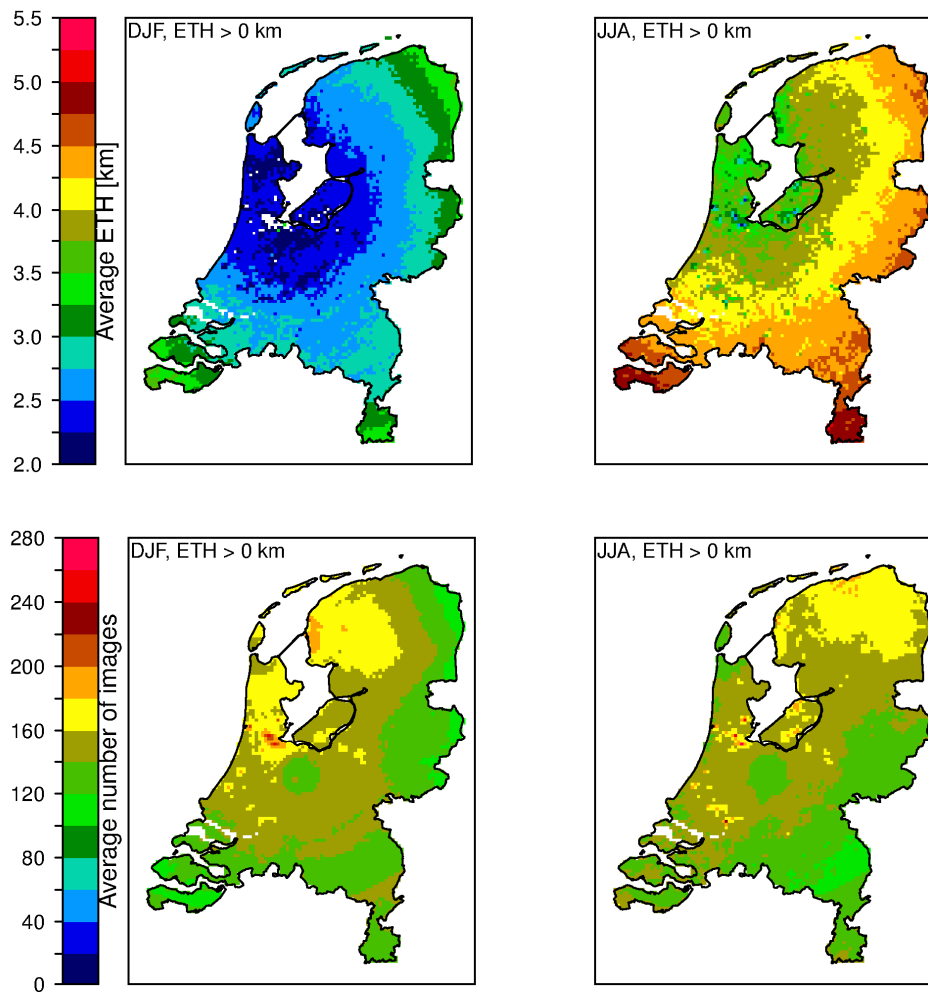


Figure 4.1 Average ETH per season for all ETH heights (ETH > 0 km) for winter (DJF) and summer (JJA) season. Upper pictures represent the average ETH. Bottom figures depict the average number of images with a rainfall depth of > 0.1 mm and ETH > 0 km.

Spring (MAM) and Autumn (SON) seasonal average ETH have a similar circular gradient, giving rise to the presumption that the spatial variability of average ETH is caused by a systematic effect. This

effect can be explained by the geometry and the volume coverage pattern (VCP) of the radar (Fig. 2.1 and 2.2). Especially during winter, ETHs are generally low and the VCP of the radar causes overestimation of ETH at far distances from the radar. Due to the earth's curvature and the geometry of the radar, the lowest (0.3°) beam of the radar is not able to measure any ETHs lower than 2 km at approximately 145 km from the radar. The maximum distance from one of the radars to a location in the country is 170 km. However, as explained in Chapter 3, the ETH radar data is based on a composite of both radar ETH data. Since the distance between the two radars is 100 km, the low average ETH surrounding both radars should be explained by another systematic phenomenon. The occurrence of (ground) clutter provides a plausible explanation. Fig. 4.1 shows that the low average ETH surrounding the Den Helder radar and north of the De Bilt radar for both seasons roughly corresponds to the low number of rainfall events on the basis of which the average ETH is calculated. The number of rainfall events is defined by the number of rainfall pixels per month on which a precipitation echo with a rainfall depth > 0.1 mm and $ETH > 0$ km is detected by the radar. The number of rainfall events appears to be highly influenced by the occurrence of clutter. All seasons show a similar pattern of rainfall events, while this would not be expected from climatology. Therefore, the described patterns are systematic and probably related to the radar artefacts.

Because of the described effects, a high number of rainfall events tend to decrease the average ETH during winter, because ETHs are generally low during this period. In the summer period a high number of rainfall events do not necessarily lead to low average ETH. It depends on the nature of the precipitating systems whether an increase in the average number of rainfall events leads to a low or high average ETH. Locations that experience frequent severe convective precipitation will most probably have higher average ETH than locations where weak convection or frontal precipitation is dominant. During summer the correspondence between average ETH and number of rainfall events indeed is less clear. This indicates that the average ETH is also associated to spatial variability in ETH due to natural variability. Finally, a circle with a radius of approximately 25 km around De Bilt and Den Helder radar stations have consistent lower rainfall events than the surrounding areas. This could be due to radar geometry prohibiting scanning of the atmosphere at more than 15 degrees angle. The radar composite should however remove underestimation of ETH and rainfall events due to the "cone of silence" (Chapter 3). This might indicate that the compositing process is unreliable.

In order to remove systematic effects, the average ETH and number of rainfall events have been calculated by removing all ETHs lower than 2 km. Most low ETHs associated to clutter will consequently be removed. During winter, removing $ETHs < 2$ km implicates the loss of some data. However, during summer, ETHs lower than 2 km will not occur frequently, and the systematic gradient due to radar artefacts will be removed to a large extent (Fig. 4.2). As a result more information about the natural variability of ETH can be extracted rather than information about radar artefacts. Additionally, $ETHs < 2$ km are not that relevant as precipitation extremes are often related to severe convection having high cloud tops, especially for sub-daily durations. Removing the $ETHs < 2$ km yields low spatial variability in average ETH during winter. The largest difference in height is in the order of 0.5 km. This could be expected since the winter period is dominated by large frontal zones and only low-topped convection due to low tropopause height. For the summer months, variability in average ETH is larger. The maximum height difference is approximately 1.5 km. The larger variability can be explained by the spatial variation in convective precipitation during summer.

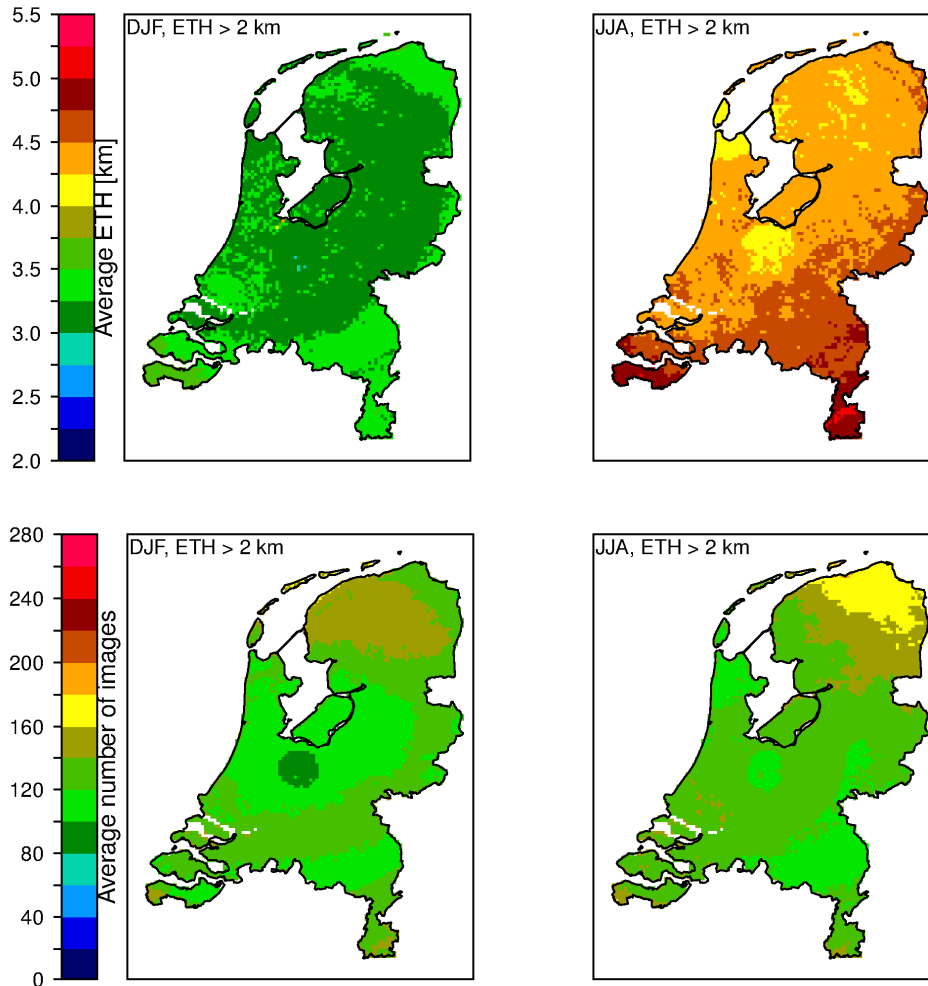


Figure 4.2 Average ETH per season for all ETH heights (ETH > 2 km) for winter (DJF) and summer (JJA) season. Upper pictures represent the average ETH. Bottom figures depict the average number of images with a rainfall depth of > 0.1 mm and ETH > 2 km.

The southeastern (SE) and southwestern (SW) part of the country experience the highest ETHs for ETHs > 2 km during summer. This is probably a result of natural variability as the southeast is the warmest area in the Netherlands during summer. However, because of the far distance from the De Bilt radar, radar artefacts will play a role as well. Interestingly, pixels at similar distance in the northeast show lower average ETH compared to the SE and SW parts. This implicates that natural variability might be the main effect in the NE part. However, further investigation of the number of precipitating events reveals that the relatively low ETHs are related to a high number of precipitating events in the NE part. This might lower the average ETH. It is complicated to distinguish between the contributions to average ETH of radar artefacts and natural variability caused by the nature of the precipitating systems. In Chapter 7 some suggestions are given to improve distinction between these two effects.

Analyses for spring and autumn show that spatial variability is relatively low, with exception of the SE part of the country. Again, this is most probably a result of the combination of both radar artefact and natural variability effects. However, if the spatial variability in average ETH would be

entirely determined by radar artefacts, locations at the same distances from the radars would show similar average ETH. This gives some credibility to the conclusion that during all seasons, except for the winter, the SE part has higher average ETHs (in the order of 1 – 1.5 km) than the rest of the country. Part of this is caused by natural variability. Spatial variability of average ETH between the other areas seems to be low (< 0.5 km).

To investigate the underlying distribution of ETH from the figures above, 6 locations in the area have been chosen. These locations are situated at various distances from the radar and in various areas of the country (table 4.1).

Table 4.1 Six locations and their respective distances (km) from the De Bilt and the Den Helder radars

| No. | Location | Distance from De Bilt radar (km) | Distance from Den Helder radar (km) |
|-----|-----------|----------------------------------|-------------------------------------|
| 1 | De Bilt | 0 | 99 |
| 2 | Purmerend | 53 | 46 |
| 3 | Zutphen | 75 | 144 |
| 4 | Hulst | 132 | 201 |
| 5 | Heerlen | 154 | 253 |
| 6 | Emmen | 150 | 136 |

The mean ETH over a 3x3 pixel square (= 52 km²) surrounding the location has been calculated to represent the locations given in Table 4.1. The cumulative frequencies of the average ETH for both winter and summer for each location are depicted in Fig. 4.3. The cumulative frequencies of the six locations are based on all 15-min radar images, except for non-existing and nodata-images. The median filter was applied to reduce the impact of spurious ETHs on the average of the 3x3-pixel block.

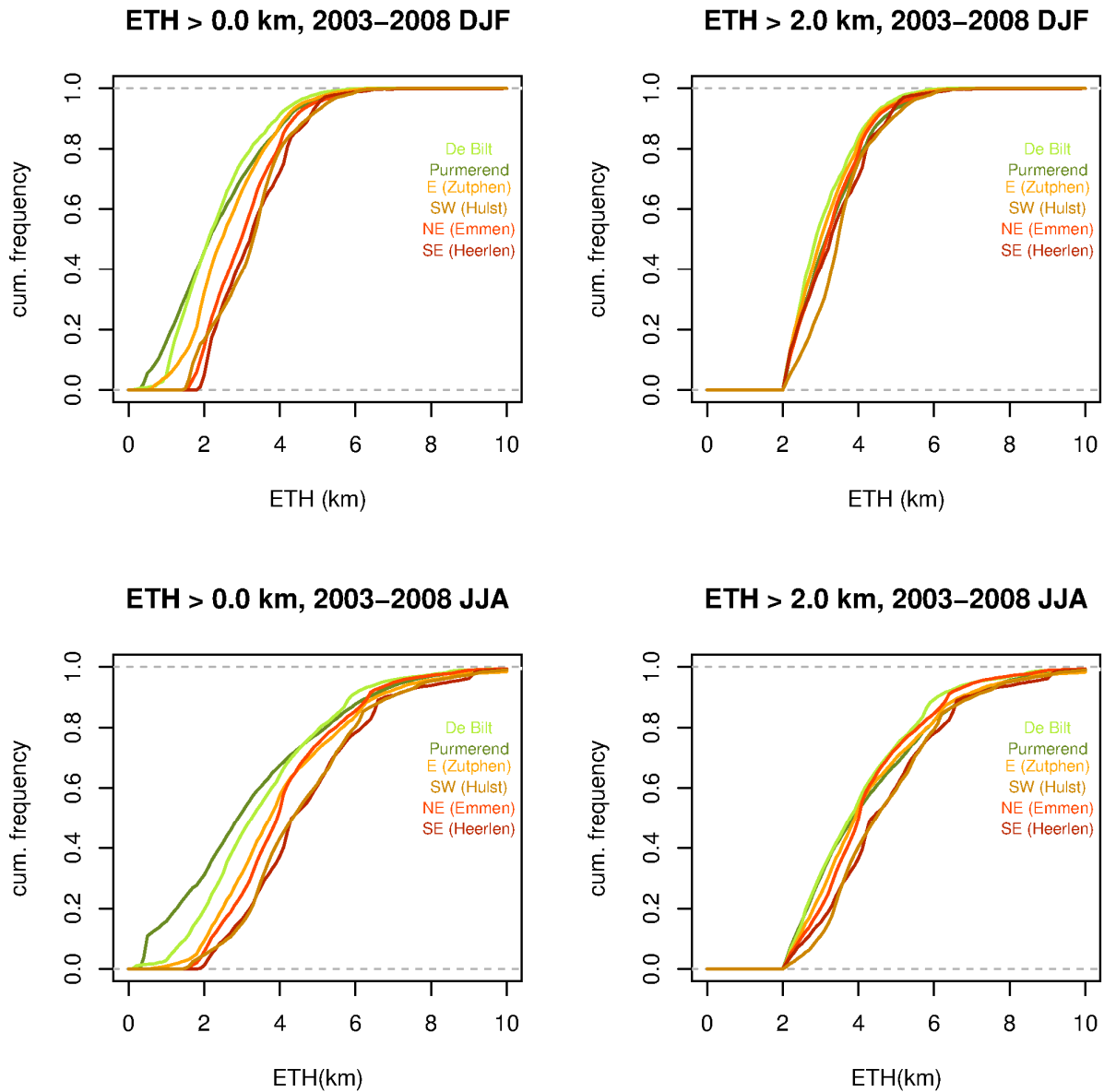


Figure 4.3 Cumulative frequencies of the ETH. Upper left = ETH > 0 km, DJF; Upper right = ETH > 2 km, DJF; Lower left = ETH > 0 km, JJA; Lower right = ETH > 2 km, JJA. Colored lines represent the six locations (Table 4.1), at ascending distance from the most distant radar. Light green = De Bilt; Dark green = Purmerend; Orange = Zutphen; Dark orange = Hulst; Red = Emmen; Dark red = Heerlen.

The cumulative frequencies for winter and summer (ETH > 0.0 km) demonstrate a gradient from low average ETH close to the radars to high average ETH at far distance from the radars. These frequencies correspond to the observed gradient of the average ETH per pixel (Figs. 4.1 and 4.2). Moreover, 40% of the average ETH is lower than 2 km for locations closer to the radar, in particular Purmerend and de Bilt, in summer. Radar artefacts should be responsible, as ETHs lower than 2 km do not occur frequently during summer. Boundary layer depth already exceeds 1 km and usually sufficient heat and moisture is available to generate deeper convection than during other seasons.

Removing the radar artefacts by removing ETHs lower than 2 km, leads to a more plausible distribution of average ETH. Most locations now show similar cumulative frequencies, which could be expected during winter. Spatial variability of average ETH is low, resulting from prevailing frontal precipitation and low temperatures. Only Hulst (SW) shows somewhat deviating frequencies. This should be attributed to natural variability. A gradient of low average ETH near the radars to high average ETH at distant locations appears during summer. Radar artefacts will be partly responsible for this effect. However, some information about the natural variability owing to the spatial characteristics of precipitating systems can be derived from Fig. 4.3. Although locations Emmen (NE), Heerlen (SE) and Hulst (SW) are at approximately the same distance from either the Den Helder or the De Bilt radar, data from 2003-2008 show that these locations have different cumulative frequencies. The SW and SE locations are characterized by higher average ETH than the NE location. The median of the latter location is approximately 0.5 km lower. This is an indication that the average ETH for the period 2003-2008 can at least partly be attributed to natural variability due to spatial characteristics of precipitating systems. This is confirmed by computing boxplots for all 6 locations for the summer period (JJA) (Fig. 4.4)

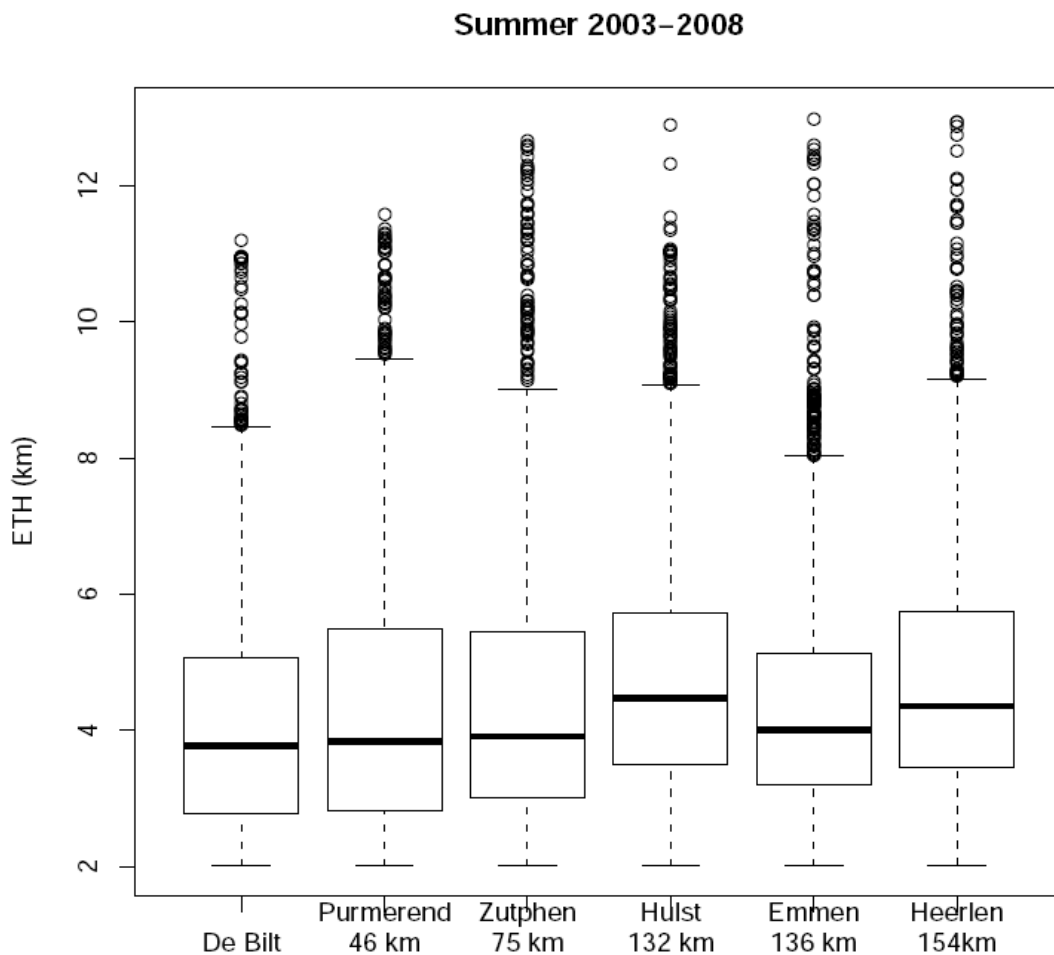


Figure 4.4 Boxplots of the six locations, showing the distributions of ETH. Horizontal bars represent the minimum and maximum (non-outlier) values. The box show respectively the first quartile, median and third quartile. Dots represent outliers.

The median of the station Hulst (SW) and Heerlen (SE) are higher in comparison with the other locations. The different distribution of Emmen (NE) suggests that natural variability at this location explains the difference in ETH distribution with the other locations (SW and SE) situated at approximately the same distance from the radar. The higher average ETHs for the SW and SE locations compared to the NE location correspond to higher average summer temperature (KNMI climatology 1971-2000) in the SW and SE locations.

4.2 Diurnal Cycle ETH 2003-2008

To explore temporal variability in ETH, the diurnal cycle for the period 2003-2008 has been calculated. The diurnal cycle has been computed for the six, spatially distributed locations as well as for all pixels over the country. The calculations are based on ETHs above 2 km only, since preceding analyses demonstrated that more information about the natural variability rather than radar artefacts could be extracted. All 15-min radar images, except for non-existing and nodata-images, were used for this analysis.

Fig. 4.5 shows distinct differences in diurnal cycle between summer (JJA) and the other seasons. The winter period (DJF) experiences only minor temporal variability in ETH. Temporal variability of ETH appears to be somewhat greater during spring and autumn. The patterns however do not reveal a clear diurnal cycle. In contrast, the summer months display the highest ETH between 15-24 UTC (=17:00-02:00 local time) for all locations. The pattern is capricious due to the small amount of pixels of each location that were used in the calculation of the diurnal cycle of average ETH. A location might experience a storm at a particular time, but another storm might miss the same location one hour later. The lowest ETHs are found during morning hours, which confirm that a diurnal cycle in the ETH occurs during summer. The pattern of high ETHs during late afternoon and evening and low ETHs found in the morning hours coincide with the highest percentage of annual 15-min and 60-min precipitation maxima in the period 1998-2008 (Overeem et al., 2009a). The largest part of those maxima occurs during the summer months. Summer precipitation is dominated by convection. The typical daily course of convection starts with the initiation of small scale convection during late afternoon. Small scale convection converges into large convective complexes. After midnight, storms weaken due to a drop in temperature and the average ETH decreases to a minimum during morning. However, frontal precipitation is usually not entirely subject to the diurnal cycle. This adds complexity to the interpretation of the diurnal cycle of the average ETH. Finally, error bars, representing one standard error, indicate that the variation around the average hourly ETH for the winter, spring and autumn season are within the range of their respective average ETH. The in general low variation in the average hourly ETH for the summer season strengthens the idea that a diurnal cycle in average ETH exists in the summer season.

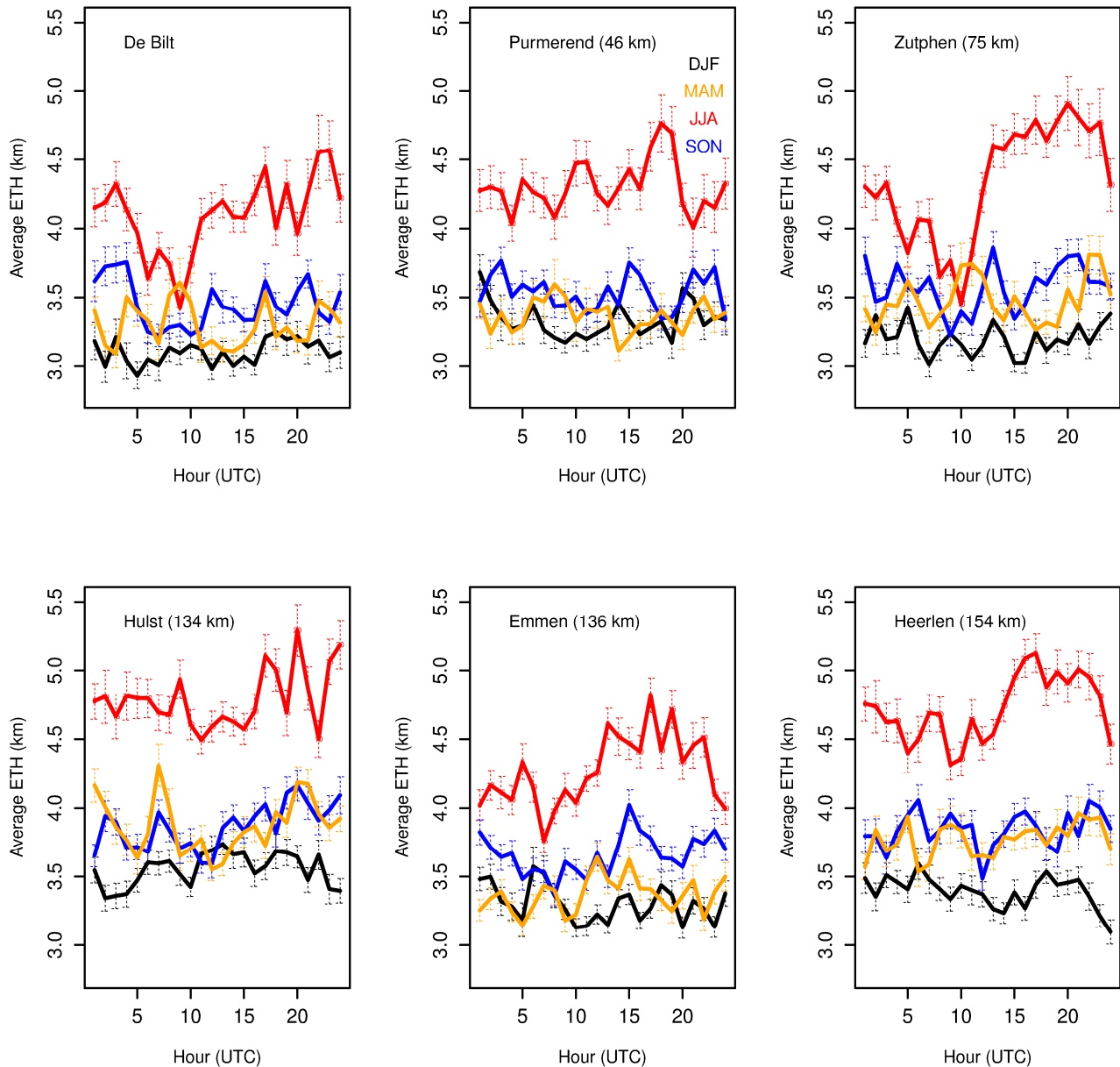


Figure 4.5 Diurnal cycle in ETH for the six locations (Table 4.1). Lines represent the average ETH per hour (Red = JJA, Blue = SON, Orange = MAM, Black = DJF). Based on 15-min ETH data for the period 2003-2008. Dashed vertical bars represent error bars of + 1 standard error and - 1 standard error.

To compensate for the capricious patterns due to the small number of pixels of each location, the diurnal cycle has been calculated based on all pixels over the country. Fig. 4.6 reveals that the highest average ETH is found during the late afternoon and early evening during the summer period, which is an indication for a diurnal cycle. The other months do not show a diurnal cycle-shaped pattern of average ETH.

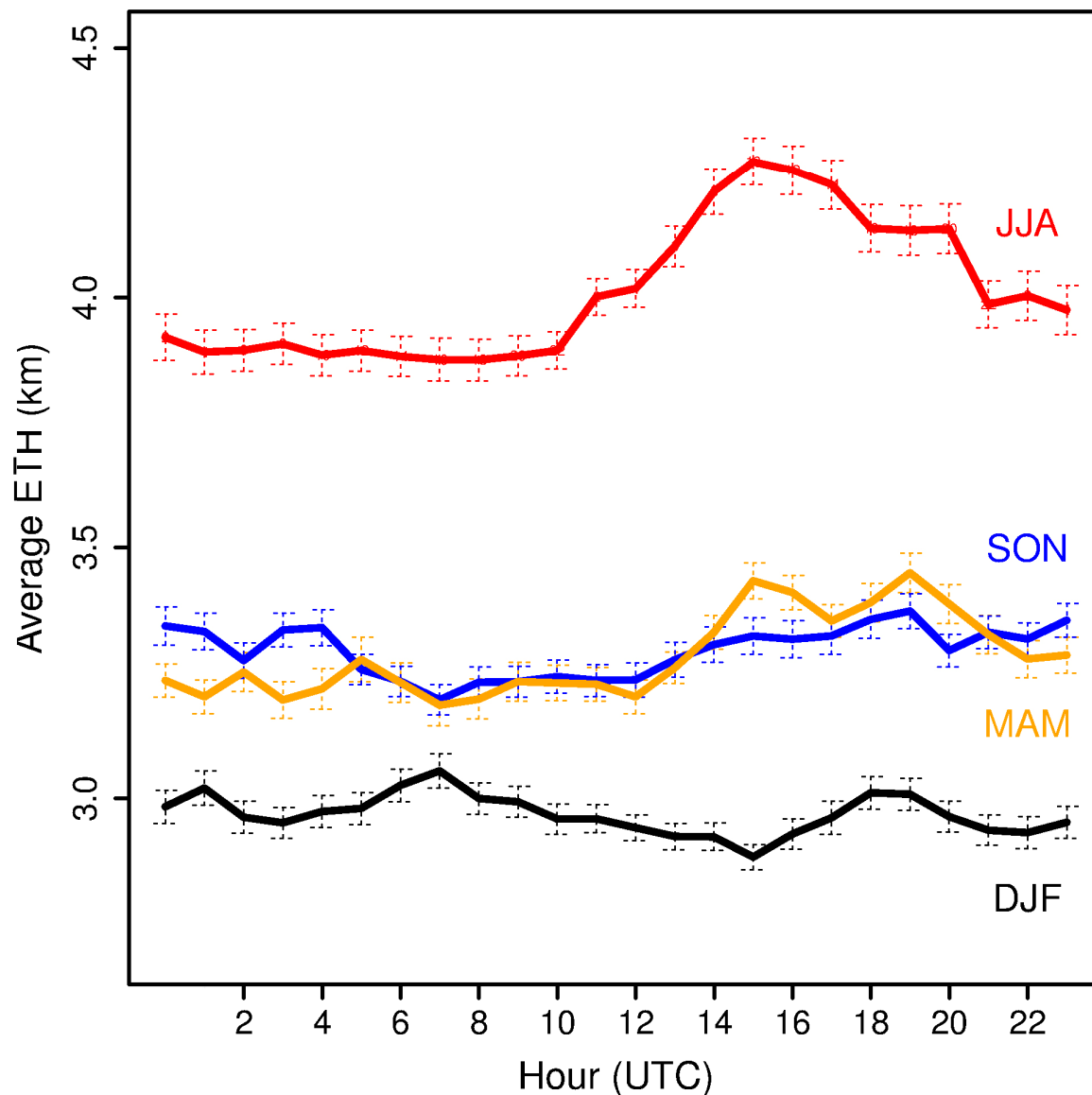


Figure 4.6 Diurnal cycle in ETH for all pixels. Based on calculation of average hourly ETH over all 15-min radar images, except for non-existing and nodata-images. Dashed vertical bars represent error bars of + 1 standard error and - 1 standard error. Colors represent seasons; Red = JJA, Blue = SON; Orange = MAM, Black = DJF.

Next, to further explore possible regional differences in the temporal variation of ETH, a spatial analysis regarding the maximum daily amplitude of the ETH is performed. The maximum daily amplitude is calculated by the maximum daily ETH - minimum daily ETH. Subsequently, the timing of the annual maximum daily amplitude has been determined for the period 2003-2008. For this analysis, the median filter has been applied to correct for spurious ETHs. These could seriously affect the maximum ETH and consequently the annual maximum daily amplitude of ETH. The average timing of the annual maxima of the daily amplitude of ETH is depicted in Fig. 4.7.

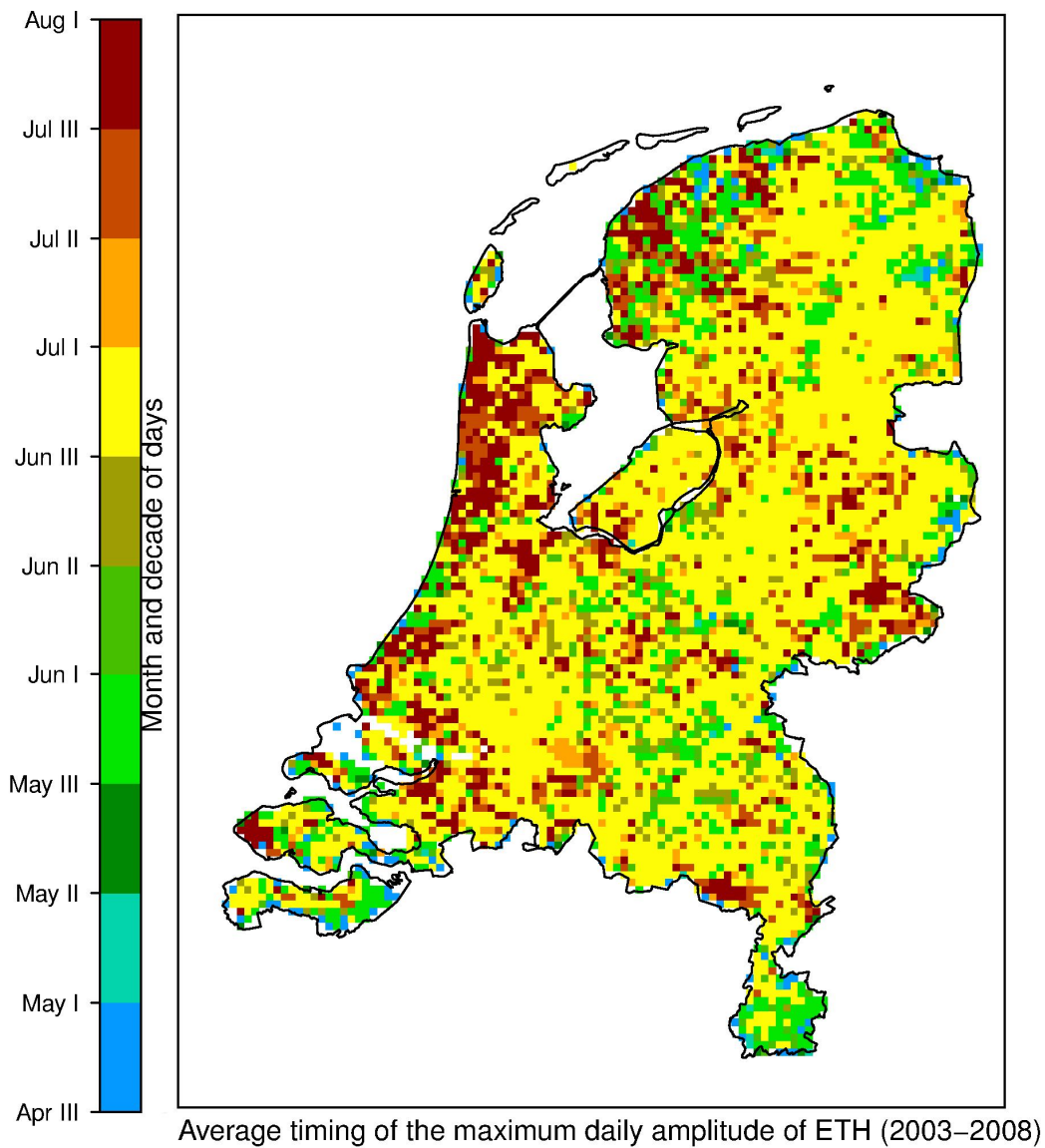


Figure 4.7 Average dates of the maximum daily amplitude (maximum ETH – minimum ETH) during the period 2003-2008. The calculation is based on all 15-min radar images, except for non-existing and nodata-images.

The average date of the annual maximum of daily amplitude does not show large regional differences (Fig. 4.7). The annual maximum mainly takes place from the third decade of May till the third decade of July. It is quite striking that the number of annual maxima steeply declines with the onset of the first decade of August. However, the daily amplitude of ETH can still be large in August. Moreover, only 6 years of data were available, which amplifies the influence on average date of an individual year. Nevertheless, the 6190 pixels representing 6190 areas of 2.5 x 2.5 km compensate for the little number of years of data available.

5. Results - Relation between ETH and precipitation intensity

5.1 Spatial and temporal correlation

The spatial squared correlation coefficient (R^2_{spat}) has been computed to assess whether the average seasonal ETH has predictive value for the average seasonal precipitation. The analysis is based on 15-min, 2.5 km resolution radar data for the period 2003-2008. The median filter was applied to remove spurious ETHs. Correlations are extremely low. R^2_{spat} is lower than 0.1 for all seasons. The average seasonal ETH does not correlate with the mean seasonal precipitation. (a) Radar artefacts, (b) the nature of precipitation systems, (c) the vertical profile of reflectivity (VPR) and (d) the geometry of a storm are probably responsible for low correlation.

Radar artefacts have caused gradually higher average ETHs for pixels located farther from the radar, as discussed in Chapter 3 and 4. On the contrary, radar artefacts likely underestimate precipitation intensity at farther distances. This effect is opposite to the assumption that higher precipitation intensity is associated with higher ETH. This will likely cause a decrease of R^2_{spat} .

The nature of precipitation systems has been discussed in Section 2.3. Here it is argued that high ETH is not necessarily connected to intense precipitation systems. Frontal precipitation usually has low to moderate cloud tops, while the precipitation intensity is generally low. Convective precipitation generally has high tops and associated precipitation intensity is high. However, frontal precipitation is often accompanied by embedded convection during summer. In winter, convection has limited depth but might produce high intensity precipitation. This all adds complexity to the relation between ETH and precipitation intensity.

The precipitation intensity throughout the vertical profile of the storm is not uniform. A storm usually shows clear gradients in the vertical profile of reflectivity. The precipitation intensity detected by the radar and processed to a radar image is attributed to different altitudes depending on the distance from the radar. Up to 15 km, the highest elevation beam is used. For the range 15-80 km the altitude at which precipitation is detected is an interpolation of the nearest elevation below and above 800 meter height (Overeem et al., 2009). The lowest elevation beam is used for detection of precipitation for distances farther than 80 km. Thus, the height at which the precipitation intensity is detected by the radar is not constant. In combination with the VPR of the storm, relating precipitation intensity to ETH is difficult. However, in this study this effect is compensated by the correction of precipitation intensity with a network of rain gauges.

Finally, the highest ETHs do not necessarily have to correspond to the highest precipitation intensity due to the geometry of the storm. Tilting of the updraft caused by windshear creates horizontal asymmetry in the storm. Anvil clouds related to CBs spread horizontally, grow in time and often have a larger surface than the surface of the precipitating cloud base. The radar might still detect high ETH within the anvil cloud, while the corresponding precipitation intensity near the surface shows large horizontal variation. Storm clouds are advected by varying windspeed at varying altitudes as well. Thus, it is not unlikely that a high precipitation intensity pixel will not correspond to a high ETH pixel for the same location.

Computation of the temporal squared correlation coefficient (R^2_{temp}) reduces the effect of some radar artefacts. The squared correlation coefficient is calculated for every single pixel. R^2_{temp} is generally low. Some months (Fig. 5.1) appears to show areas with higher correlation, which will be discussed in more detail.

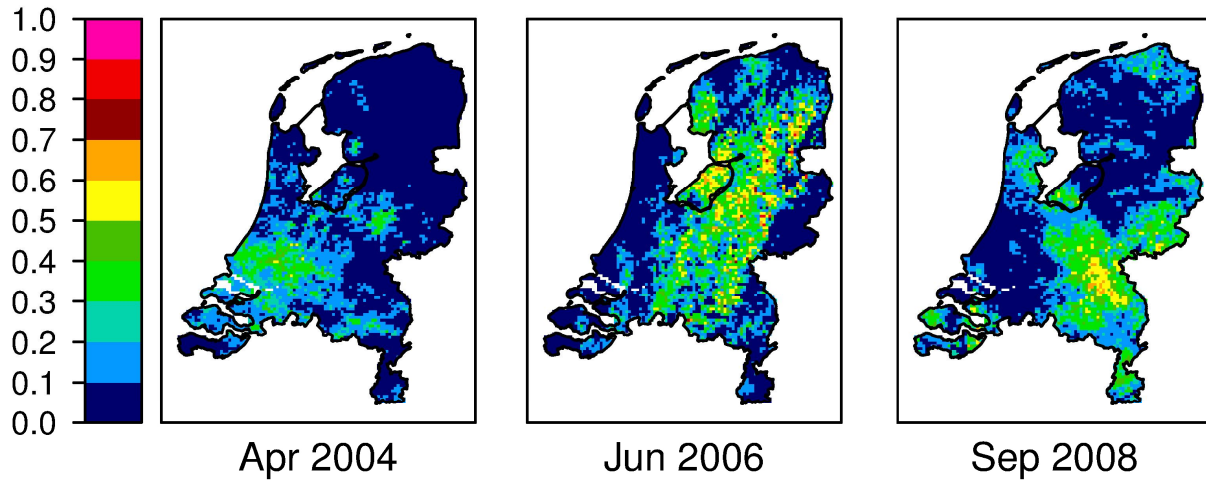


Figure 5.1 Temporal squared correlation coefficient (R^2_{temp}) for every single pixel for April 2004, June 2006 and September 2008. The calculation is based on all 15-min, 2.5 km radar images, except for missing images and nodata-images. Reddish colors indicate higher correlation than green and blue pixels.

All three months have experienced lower rainfall compared to the rainfall climatology. The higher values of R^2 during April 2004 appear to correspond with two severe convective situations (28 and 30 April) over the southwestern part of the Netherlands. For June 2006, an extremely dry month, high values of R^2 over the central and eastern part show correspondence with convective events over these areas, while the western part has experienced mainly frontal precipitation. These months seem to indicate that the ETH has some predictive value for the precipitation intensity. Relatively strong correlation for some areas in September 2008 cannot be related to convective events. Here, stronger correlations might be linked to an area of convective precipitation from the southwest to the northeast of the country.

To reduce the effect of different precipitation systems (stratiform - cumuliform) to the relation between ETH and precipitation intensity and to study whether the relatively strong correlations are associated with convective events, a case study for the 2010 summer period is presented in the next section.

5.2 Case study summer 2010

In Fig. 5.2 the average ETH, monthly precipitation and the temporal squared correlation coefficient (R^2_{temp}) are depicted for each month. The calculation is based on 5 min, 1 km resolution radar data for the period June – August 2010. Only ETHs > 2.0 km are used. The median filter was utilized to remove spurious ETHs. For this period, observations by a weather forecaster of cumulonimbus clouds were available to select convective rainfall events. In June 1344 5-min radar images showed the occurrence of CBs. For July 2448 5-min radar images were selected based on the observations of the weather forecaster, while August 2010 contains 3948 convective 15-min observations. This corresponds to 15% of the total time in June, 27% of July, 44% of August.

June 2010 was overall dry with only a small number of rainfall events, associated with frontal zones, producing only light to moderate convection. On only two days, severe convection was observed by the weather forecaster. The corresponding average ETH is relatively low with tops ranging from 3.5 - 5.0 km height. The spatial squared correlation coefficient ($R^2_{spat} = 0.14$) as well as the temporal

squared correlation coefficient (R^2_{temp} , Fig. 5.2) are low. July 2010 is characterized by some events with severe convection observed by the weather forecaster, especially during the period July 10-14th. On 17 days thunderstorms were observed over the country. The average ETH is relatively high, ranging from 5-8 km. The spatial squared correlation coefficient is very low ($R^2_{spat} = 0.1$). R^2_{temp} is somewhat higher for some parts in the west of the country. Nevertheless, the ETH does not seem to be an important predictor for precipitation intensity in July 2010. August 2010 is dominated by numerous days with mostly moderate to high intensity rain showers. Prevailing winds from the west led to convection mainly in the polar air. On the contrary, the storms occurring in July 2010 mainly developed in very warm and moist air conveyed by prevailing southerly winds, probably leading to a higher mean ETH.

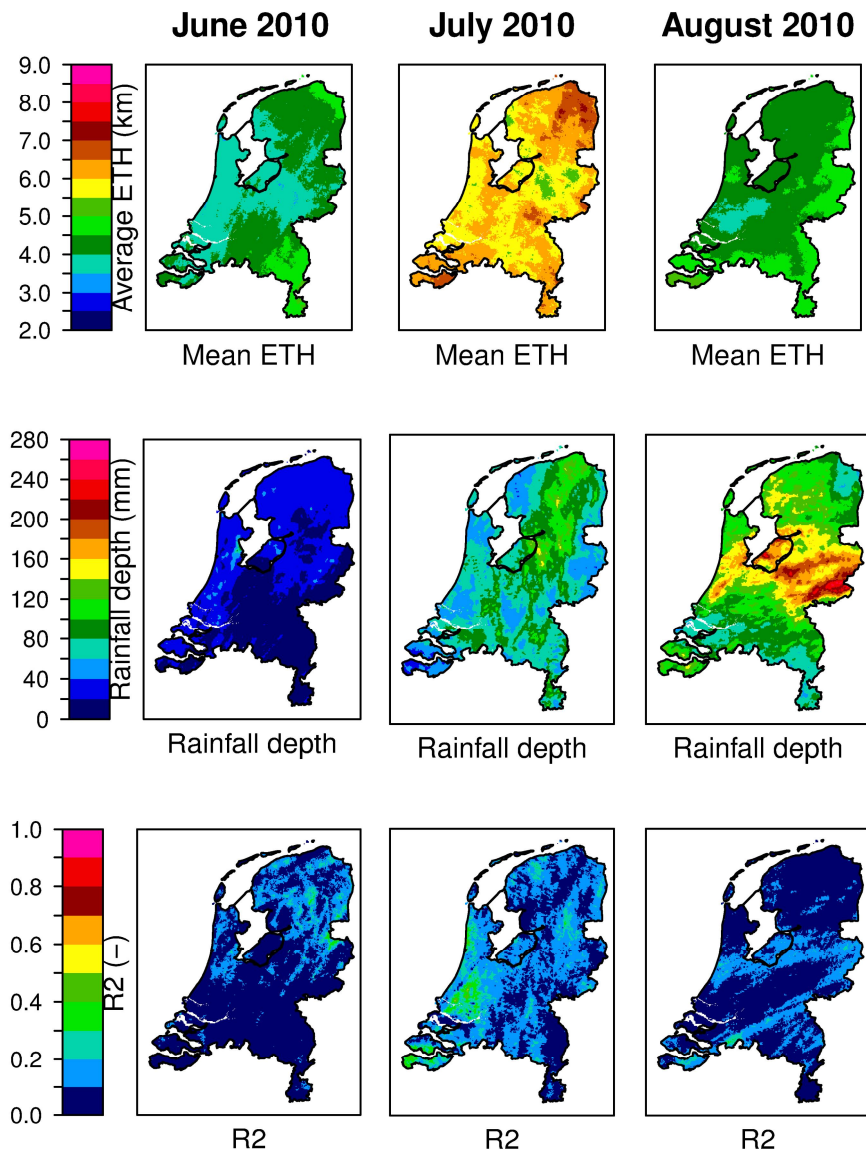


Figure 5.2 Mean ETH, Rainfall depth and R^2_{temp} for the months of June, July and August 2010. The upper row pictures depict the average ETH (km), the middle row pictures show the accumulated rainfall depth (mm) and the lower row pictures present the R^2_{temp} . Based on 5-min, 1 km resolution precipitation and ETH data for convective events that were observed by a weather forecaster.

The type of air mass determines the height of the tropopause and consequently the maximum height of a storm. This is nicely illustrated by the average ETH for July and August. The average ETH in August is approximately 1 to 3 km lower than the average ETH in July 2010. Convection in a polar air mass has lower ETH than convection developing in a tropical air mass. The average temperature in July and August 2010 in De Bilt was respectively 19.9°C and 16.8°C. Both squared correlation coefficients for August 2010 are extremely low and do not provide any indication that ETH is a predictor for precipitation intensity. The low correlation between the ETH and precipitation intensity can be attributed to the four factors discussed in the previous section, namely radar artefacts, the nature of precipitation systems, the vertical profile of reflectivity (VPR) and the geometry of a storm. By selecting only convective precipitation, distortion of the correlation because of several types of precipitation reduces. However, convection seems to be associated to a wide range of precipitation intensities.

It was already explained that the calculation of the temporal squared correlation coefficient is prone to the geometry of a storm. It is not very likely that a high ETH will always coincide with a high precipitation intensity pixel. A cell recognition algorithm was utilized to detect connected pixels of rainfall depth > 0.1 mm. These recognized cells are combined with the ETH data to gain information about the ETH characteristics of a storm cell. The correlation between the maximum ETH and the maximum precipitation intensity for recognized storms in the period June – August 2010 is depicted in Fig. 5.3.

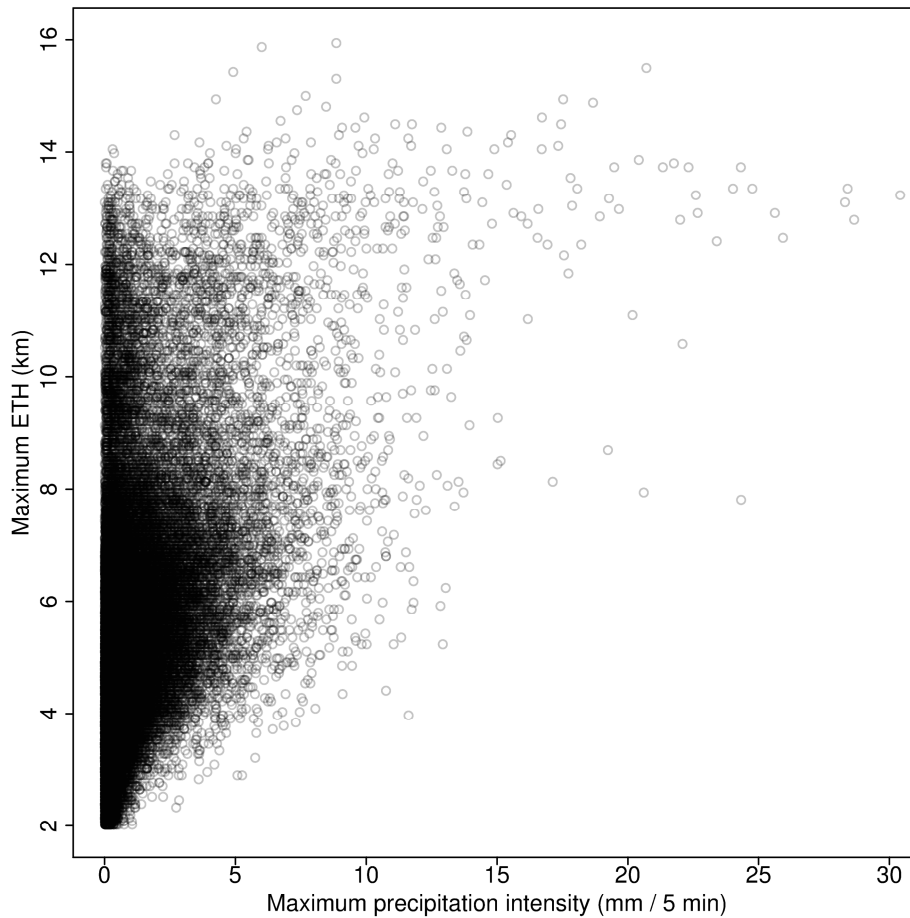


Figure 5.3 Scatter plot of the maximum ETH versus the maximum precipitation intensity. Based on observed convection by a weather forecaster for a 5-min, 1-km resolution data set of ETH and precipitation intensity. The maximum ETH and precipitation intensity are properties of storm cells recognized by utilizing a cell recognition algorithm.

For this purpose, 5-min, 1 km resolution data for selected convective events by the weather forecaster for the period June – August were used. Only ETHs > 2 km are used. A median filter was applied to remove spurious echoes. Fig. 5.3 shows that the correlation between the maximum ETH and maximum precipitation intensity of a recognized cell for selected convective rainfall events is low. The squared correlation coefficient for a linear relation and power-law relation is respectively 0.234 and 0.244. Although the squared correlation coefficient is low, it seems to be a clear indication that intense precipitation events (> 15 mm per 5 min) are always associated by relatively high ETHs (> 8 km).

6. Discussion

6.1 Spatial and temporal variability of ETH

It has been argued that the spatial and temporal variability of ETH of storms is subject to three main factors. The first is the natural variability due to precipitation systems having certain cloud tops. The resulting spatial and temporal variability of ETH is seriously affected by the other two factors, namely the radar artefacts due to the detection of ground clutter and the scanning geometry of the radar.

The detection of ground clutter causes a systematic decrease in average ETH near the radar. Application of a precipitation filter, based on a clutter-corrected precipitation intensity data set, reduces the amount of ground clutter to a large extent. However, it is argued that existing ground clutter still has impact on the average ETH near the radar, because a large amount of unrealistic low ETHs are included. A possibility to correct for ground clutter is the increase of the detection threshold for precipitation intensity. For this study, the threshold of 0.1 mm h^{-1} has been taken for the precipitation intensity data set. Nevertheless, the effective threshold will often be somewhat higher since the precipitation intensity data set was corrected by data from rain gauges. Ground clutter is usually characterized by very low ETH or high precipitation values, which are excluded by an increase of the threshold. However, the choice of the value of the threshold is arbitrary and it could lead to excluding valid data unintentionally. A sensitivity study for the value of the detection threshold should then be performed.

In this study, only ETHs higher than 2 km have been included in the computation of the spatial and temporal variability of ETH. This will remove the largest part of (ground) clutter. This method will possibly also exclude valid ETH data. However, ETHs lower than 2 km are not associated with high intensity precipitation events. Moreover, results have also shown that a high number of radar images correspond to lower average ETH. During all seasons, there is a tendency that an increase of the number of radar images leads to a decrease in average ETH. The average ETH of the summer months (JJA) provides a clear example.

The average seasonal ETH as well as the cumulative distributions of six locations showed that artefacts due to the scanning geometry of the radar affect the spatial and temporal variation in ETH. The scanning geometry leads to overshooting of tops due to the curvature of the earth and incorrect elevation detection because of the increase of the beam volume and the limited number of elevations. This has been manifested by the gradual increase of average ETH for increasing distance from the radar. Moreover, single ETH radar images as well as the average ETH systematically show “rings” of higher and lower ETHs, owing to the increase of the beam volume and limited number of scanning elevations. Since these effects are inherent to the physical and geometrical construction of the radar, reducing these effects is difficult. From 2008 onwards, a new radar system has been installed that improved the number of low and high elevation scans. The number of total elevation scans has not been increased. A quick look at the average monthly ETH for 2009 does still show the gradual increase and rings of higher and lower ETH. The distinct gradient of average ETH leads to the question whether the compositing of radar images of both radar stations works correctly. The metadata of the ETH HDF5 files do not give a definitive answer. Evaluation of 4 stratiform and 4 convective rainfall events show that at least 2 stratiform events seem to show remarkably lower ETHs near the radars. This is especially true for the De Bilt radar. A frontal zone on December 28, 2004 has been studied in more detail. Radar images on 04:02 AM and 06:47 AM are depicted in Fig. 6.1.

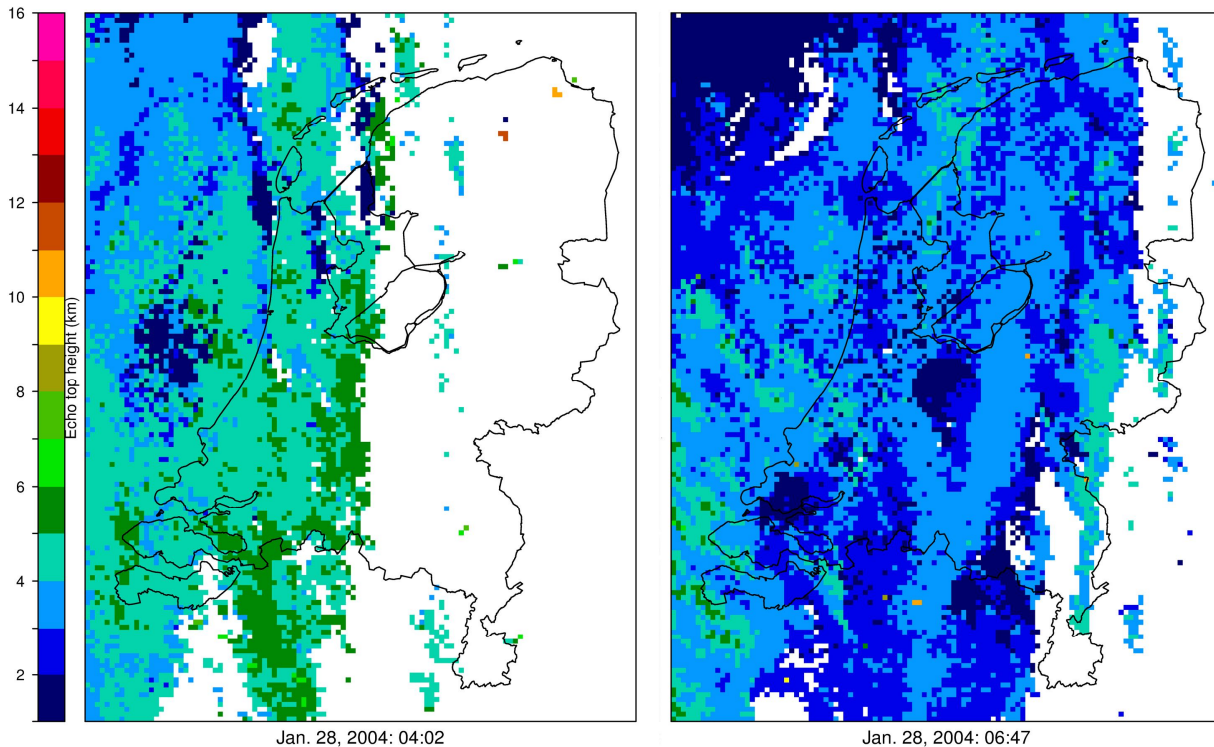


Figure 6.1 Raw 15-min, 2.5-km ETH data for a frontal zone bringing snow on 28-12-2004. The first image is on 04:02 UTC, the second on 06:47 UTC. Blue colors represent ETHs < 4 km, green colors represent ETHs of at least 4 km.

From 05:45 UTC the radar images suddenly show a circle of lower ETHs than surrounding pixels around the De Bilt radar. An example is given for 06:47 UTC. At 04:02 UTC this feature is not visible. The composite should always take the highest tops and should consequently yield ETH of approximately 3 km instead of 1 km. The dynamical nature of convective storms makes it much more difficult to assess whether a similar feature occurs for convective precipitation. Finally, it is difficult to distinguish real natural variability from the effects from the radar artefacts described in this section. Verifying the results is rather difficult as well, as a comparable study about the spatial and temporal variability of cloud top height has not yet been performed to the author's knowledge.

The ETH is not equal to the actual cloud top height. The radar is not able to detect very small droplets. The actual cloud top may consist of very small droplets and as a result the ETH is lower than the actual cloud top height. The detection threshold by the radar determines what distribution of droplets can be detected. For this study 7 dBZ is taken. Other studies (such as Maddox et al. 1999) using the WSR-88D radars, use 18.5 dBZ as the detection threshold.

Other methods are available for the measuring of the actual cloud top height. Takacs et al. (2005) describes the estimation of cloud top height by combining satellite-derived cloud top temperature and information from vertical temperature profiles calculated by numerical prediction models. Randriamampianina et al. (2000) use the same approach and compare the satellite-derived cloud top heights with the radar-based ETHs. They find good agreement for single-layer clouds for distances up to 100 km from the radar. Holland et al. (2006) find that cloud tops are consistently higher than ETHs for all cloud types in the 4.5 – 13.5 km vertical range, using a cloud top product that is also based on satellite-derived cloud top temperature and a vertical temperature profile. Wang et al. (2000)

presents an analysis of the vertical dimension of clouds using a 20-year radiosonde data set. They find an average global cloud top height of 4.0 km. Pilot reports can provide information on cloud tops as well (Takacs et al., 2004). The use of data from satellites, radiosondes and vertical temperature profiles has important drawbacks. Some satellites as well as radiosondes have low temporal resolution. The latter has low spatial resolution as well. Calculation of vertical temperature profiles is based on numerical prediction models and induces uncertainty. However, these methods, from which cloud top heights can be computed, are able to measure cloud tops instead of echo tops. It depends on the purpose of the study which method is most suitable. Satellite data, vertical temperature profiles and radiosondes can provide useful data to verify ETHs and vice versa.

Finally, it should be stressed that this report has not calculated a climatology. Six years of data is too short for this purpose. Individual extremes can have important influence on the average ETH. The calculation of the average timing of the annual maximum of the daily amplitude of ETH, for instance, is based on only 6 years of data. Nonetheless, the high resolution of the data used makes it possible to explore spatial and temporal variability of ETH on a very small scale.

6.2 Implications for the operational use of the ETH product

The ETH radar product is used operationally by the KNMI forecasting department as well as by the Air Traffic Control of the Netherlands. Selected ETHs are displayed on the operational radar image display (Fig. 6.2).

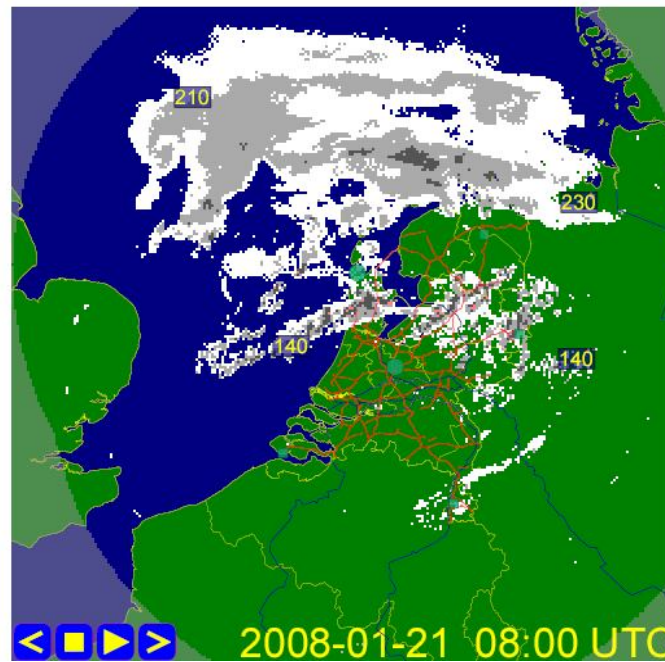


Figure 6.2 An example of an operational radar image display as used at the KNMI forecasting department. The radar displays precipitation echoes as well as maximum ETH of selected cells. Notation of maximum ETH is in flight level units (hFt).

The method for selection of ETHs is described by Holleman (2008) and is summarized in short. From the radar ETH images, as used for this study (see Fig. 6.1), only the highest tops are selected. This

selection is based on cell identification. A group of connected pixels is defined as a cell. ETH pixels lower than a threshold are excluded. This threshold is calculated by taking the 25% highest ETHs from all ETH pixels at a certain time. Only cells consisting of ETH pixels higher than the threshold are identified. Next, the maximum ETH of the identified cell is annotated and projected on the operational weather radar image display. Note that the annotated echo top heights are converted into flight level units (hFt), whereby $ETH (hFt) = ETH (km) / 32.9$.

The radar artefacts as discussed in the previous section are applicable to the operational use of the ETH product as well. Since only the maximum ETH is selected, the annotated ETHs are prone to the increase of beam filling, gaps in the scanning elevations, deviations from normal refraction and the detection of non-hydrometeors. The latter spurious echoes are removed by a smoothing filter that evaluates the neighboring 8 cells. Errors in the annotation of ETH are not expected to hamper the operational use for daily weather significantly. The relative growth and decay of storms and related increase and decrease of the ETH are most probably more important than monitoring of the absolute ETH. However, for aviation purposes, errors in the annotation of ETH could sometimes be dangerous. NASA (1997) indicated that errors up to 1.2 km occur due to deviation from normal atmospheric refraction. The use of satellite data and detection of cloud base and thickness of layers by using LIDAR might then be more appropriate, especially because these methods are capable of measuring cloud top height instead of ETH.

6.3 Relation between the ETH and precipitation intensity of storms

Analyses of the relation between the ETH and precipitation intensity of storms have been performed in a range of spatial and temporal scales. In general, the correlation is low. This is due to radar artefacts, the nature of precipitation systems, the vertical profile of reflectivity and the geometry of a storm. However, the results indicate that the ETH has some predictive value for precipitation intensity for pure convective precipitation, e.g. where no stratiform precipitation is incorporated. Direct correlation between cloud top height or ETH and precipitation intensity has been evaluated by only few studies and mostly for tropical thunderstorms. Gagin et al. (1984) presents an analysis of the relationship between the height of a convective cell and its precipitation characteristics in South Florida. The analysis was confined to single convective cells rather than multicellular convective systems, wherein stratiform rain is often observed as well. They found that rainfall intensity, as well as other precipitation characteristics, are strongly dependent on the height of convective cells. The relation appears to take the form of power laws. This study has not found a relation based on a power law between ETH and precipitation intensity. The squared correlation coefficient is 0.244. This could be because the observations of convective precipitation by the weather forecaster do very likely not consist of only pure convective rainfall, which is the case in the analysis of Gagin et al. (1984). Gagin et al. (1984)'s analysis further suggests that the depth of convective cells is associated with larger total rain volumes due to higher precipitation intensity, longer lifetime and larger precipitation areas. Interestingly, a positive relation exists between the vertical and horizontal dimension of convective storms. A radar-equipped airplane was available for detecting precipitation and ETH echoes in Western-Pacific tropical convection (DeMott and Rutledge, 1997). The analysis shows that the instantaneous correlation between precipitation intensity and ETH is 0.55, but large scatter is observed around this value. The correlation of precipitation intensity with the 30-dBZ contour shows to be much stronger. This 30-dBZ contour level is linked to internal microphysical properties and lightning within a cloud. It is argued that due to the much stronger correlation of the 30-dBZ contour level, the ETH is only a partial determinant of precipitation intensity.

The question is raised whether a uniform relation exists between the vertical dimension of storms and their precipitation intensity for different climates and different seasons (Gagin et al., 1984). A review of observational radar studies of the relation between cloud height and precipitation intensity and volume of thunderstorms, is given by Adler and Mack (1984). This review includes analyses for different climatic regions. They argue that the ETH is strongly correlated to the maximum precipitation intensity in a specific climate. However, they show that there is a larger variation in the relation ETH – precipitation intensity for climates characterized by a more unstable, dry climate compared to climates having a more stable and moist lapse rate. This result also suggests that seasonal variation in atmospheric stability and moisture content influence the ETH – precipitation intensity relation, even within a climate zone. Nevertheless, the ETH – precipitation intensity relation analyzed by this study is primarily intended for the Netherlands. Literature supports the assumption that the weak correlation between ETH and precipitation intensity found in Chapter 5, is mainly related to the occurrence of both stratiform and convective precipitation.

7. Conclusion and recommendations

The so-called echo top height of a storm is the maximum height of a precipitation echo and therefore a measure for its vertical extent. Severe storms are characterized by a large vertical extent and are not seldom associated with high precipitation intensity. Echo top height (ETH) data, with a spatial and temporal resolution of respectively 2.5 km and 15-min, for the period 2003-2008 were available to investigate the spatial and temporal variability of ETH. This study presents a unique multi-year analysis of the spatial and temporal variability of ETH and its relation with precipitation intensity. Moreover, an evaluation of the error sources affecting the ETH radar product, contributes strongly to the understanding of the ETH radar product. The analysis of the ETH variation and ETH-precipitation intensity relation and the evaluation of error sources is relevant to aviation and the understanding of the relation between the vertical dimension of a storm and precipitation extremes.

The spatial variability of the ETH is affected by radar artefacts, which makes identification of spatial variability due to the movement and character of precipitation systems difficult. However, the underlying distributions of ETH for six locations in the Netherlands have shown that the highest ETHs can be found in the southwest and southeastern part during summer, possibly owing to the highest average temperature observed in these parts. The spatial variation in winter, spring and autumn is small. The temporal variation of ETH has been analyzed by computation of the diurnal cycle. Results indicate that the average ETH peaks during late afternoon and evening for the summer period. A diurnal cycle seems to be absent during other seasons. Average timing of the annual maximum daily amplitude (maximum ETH – minimum ETH) occurs in the period June-July.

The relation ETH – precipitation intensity has been reviewed on different spatial and temporal scales. The spatial squared correlation coefficient shows a weak relation between ETH and precipitation intensity for all seasons. The temporal squared correlation coefficient shows overall weak correlation. However, some months, characterized by severe convective events, seems to show somewhat stronger correlation between ETH and precipitation intensity. This is in accordance with existing studies, stating that dependence of precipitation intensity on the vertical extent of storms is found for pure convective cells. A case study for the summer of 2010, using high resolution data (5 min, 1 km), based on the observed convective clouds by a weather forecaster, has therefore been conducted to distinguish convective from stratiform precipitation. The correlation is still weak, probably related to radar artefacts and embedded stratiform rain in convection.

Although the results of this study seem to be seriously affected by radar artefacts, a unique

multi-year, high resolution analysis of the spatial and temporal variability of ETH and its relation with precipitation intensity has been presented. The evaluation of error sources affecting the analysis produced a wealth of information that is relevant to the operational use of the ETH for nowcasting weather and aviation. Finally, some recommendations are given in order to perform a more in-depth study.

- ♣ An effort should be undertaken to distinguish radar artefacts from real natural variability of ETH.
 - To reduce the impact of clutter, the value of the corresponding precipitation intensity should be increased to values higher than the detection threshold of 7 dBZ (≈ 0.1 mm/h).
 - The application of the cell recognition algorithm described in Section 3.4 can further reduce the impact of clutter. Setting a minimum area of connected cells should remove clutter.
 - The impact of errors sources on ETH should be quantified. This could be done by verification with satellite-derived cloud top heights, vertical temperature profiles based on numerical prediction models and measurements by radiosondes.
 - The use of a composite from Belgian or German radars could decrease overshooting and beam filling effects.

- ♣ Statistical tests should be performed to quantify possible regional variability in ETH.

- ♣ The relation ETH – precipitation intensity can be improved:
 - An algorithm should be used to distinguish stratiform and convective precipitation to gain better relationships between intensity – ETH. A useful algorithm has been developed by Steiner et al. (1984).
 - Volume radar data can be used to gain information on the vertical profile of reflectivity of a storm. Since a clear gradient in the vertical profile of reflectivity is usually present in a storm, volume radar data can be used to locate the precipitation cores and associated cloud tops more accurately.

- ♣ Indirect relations between ETH and precipitation intensity provide further understanding between the storm's vertical dimension and precipitation intensity. Lenderink et al. (2011) shows that a positive correlation exists between the dewpoint and precipitation intensity. Atmospheric stability and moisture content are the main determinants of a storm's ability to develop strong updrafts. Therefore, a relationship between dewpoint and the vertical dimension of storms seems plausible.

- ♣ Further understanding of the vertical dimension of storms, which can be gained by relating the ETH to other precipitation characteristics. Gagin et al. (1984) presents an analysis of the vertical dimension in relation to the total volume of precipitation in a storm, the storm's lifetime and time to reach maximum ETH or maximum precipitation intensity. Moreover, the vertical integrated liquid content of a storm can be related to the ETH.

- ♣ The horizontal dimension of storms most probably is related to precipitation intensity as well. The cell recognition algorithm discussed in Section 3.4 can be used for this purpose. Gagin et al (1984) and Simpson and Woodley (1971) show that the horizontal dimension of rainstorms is positively correlated with the accumulated precipitation and lifetime of the storm.

Dankwoord. Als eerste wil ik Aart Overeem bedanken voor zijn begeleiding van mijn stage op het KNMI. Zijn hulp bij de gebruikte C- en R-scriptjes voor mijn analyse was ontzettend waardevol en soms ook noodzakelijk. Ik kon altijd bij je terecht met vragen over zowel de inhoud als de opmaak van dit rapport. Misschien nog belangrijker was jouw geloof in de goede afloop, waar ik die soms aan het verliezen was. Dank ook voor de fijne gesprekken over non-meteorologische of hydrologische zaken! Ik wil ook Hidde Leijnse bedanken voor zijn enorme enthousiasme en talloze waardevolle suggesties. Door je droge humor was het altijd goed om tijdens de lunch aan je tafel te kunnen zitten. Ik dank ook Remko Uijlenhoet (WUR). Ondanks zijn krappe agenda, heeft hij iedere keer betrokkenheid getoond bij mijn stage en me voorzien van enkele waardevolle suggesties. Verder dank ik Pieter Arts (KNMI) voor het beschikbaar stellen van de dataset met observaties van convectieve bewolking. Ik wil Hans Beekhuis bedanken voor de rondleiding in de radartoren. En tenslotte mijn (helaas) ex-collega's op de afdeling weeronderzoek. Ondanks een rustige en soms saaie zomerperiode heb ik me ontzettend op mijn gemak gevoeld. De relaxte werksfeer, inspirerende omgeving en goede contacten doen me terugblikken op een goede tijd op het KNMI.

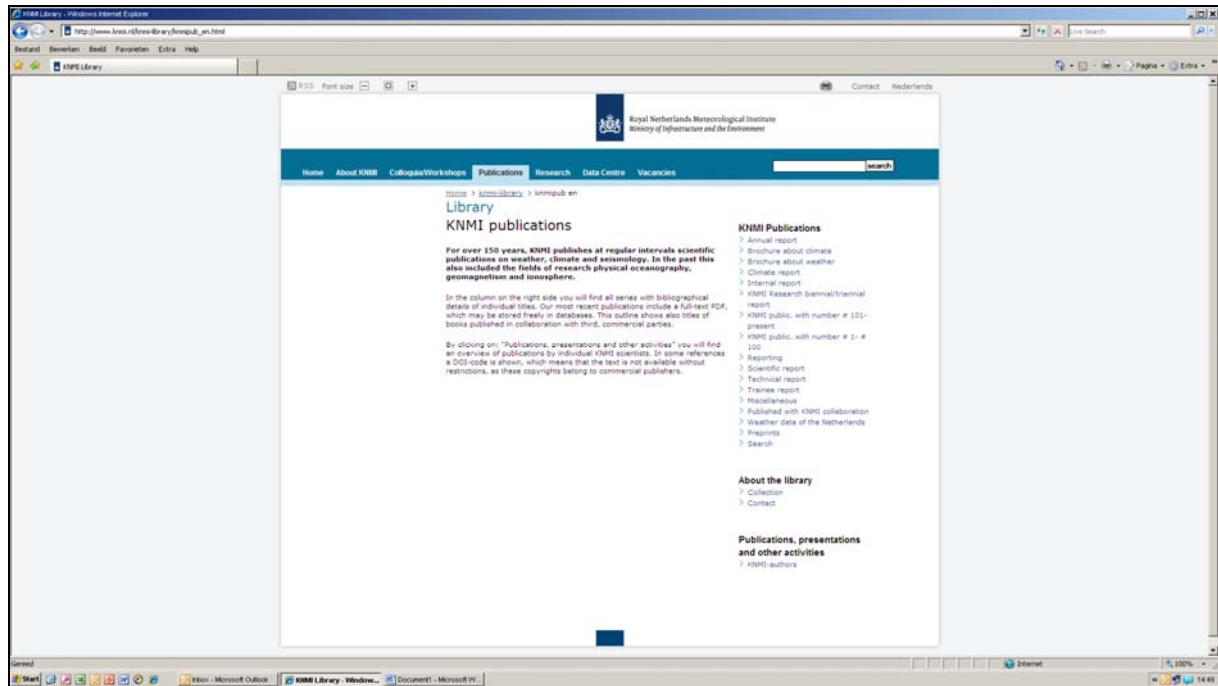
References

- Adler, R.F., and R.A. Mack (1984), Thunderstorm height/rainfall rate relations for use with satellite rainfall estimation techniques, *Journal of Climate and Applied Meteorology*, 23, pp 280-296.
- Beekhuis, H. and I. Holleman (2010), *From Pulse to Product, Highlights of the digital-if upgrade of the Dutch national radar network*, KNMI, De Bilt.
- DeLobbe, L. and I. Holleman (2006), Uncertainties in radar echo top heights used for hail detection, *Meteorological Applications*, 13, 361-374.
- DeMott, C.A. and S.A. Rutledge (1997), The vertical structure of TOGA COARE convection. Part 1: Radar echo distributions, *Journal of the Atmospheric Sciences*, 55, pp. 2730 – 2747.
- Gagin, A., D. Rosenfeld and R.E. Lopez (1984), The relationship between Height and Precipitation Characteristics of Summertime Convective Cells in South Florida, *Journal of the atmospheric sciences*, 42:1, pp. 84-94.
- Holland, L., A. Takacs, B. Brown, E. Gilleland, R. Huefle and J. Wolff (2006), *A comparison of the cloud top height product (ctop) and cloud-topheights derived from satellite, rawinsonde, and radar*, report p1.21a, Research Applications Laboratory, National Center for Atmospheric Research, Boulder, CO, USA.
- Holleman, I. (2006), *Bias adjustment of radar-based 3-hour precipitation accumulations*, Technical Report TR-290, KNMI, De Bilt.
- Maddox, R.A., D.S. Daras, P.L. MacKeen, J.J. Gourley, R. Rabin and K.W. Howard (1999), Echo Height Measurement with the WSR-88D: Use of data from one versus two radars, *Weather and Forecasting*, pp 455-460.
- Marshall, J.S., W. Hirschfeld and K.L.S. Gunn (1955), Advances in radar weather. *Advances in Geophysics*, 2, pp 1-57.
- Michelson, D., T. Einfalt, I. Holleman, U. Gjertsen, K. Friedrich, G. Haase, M. Lindskog, and A. Jurczyk (2005): *Weather radar data quality in Europe: Quality control and characterization*. Technical Report EUR 21955, EU (Brussels), 92 pp.
- NASA (1997), *Report on the Radar/PIREP Cloud Top Discrepancy Study*, NASA Contractor Report CR-204381, pp. 18.
- Overeem, A., A. Buishand and I. Holleman (2009a), Extreme rainfall analysis and estimation of depth-duration-frequency curves using weather radar, *Water Resource Research*, 45, 15 pp.
- Overeem, A., A. Buishand and I. Holleman (2009b), Derivation of a 10-year radar-based climatology of rainfall, *Journal of Applied Meteorology and Climatology*, 48, pp 1448-1463.
- Randriamampianina, R., J. Nagy, T. Balogh and J. Kerenyi (2000), Determination of Cloud Top Height Using Meteorological Satellite and Radar Data, *Phys. Chem. Earth (B)*, 25, No. 10-12, pp. 1103-1106.2000.

- Rinehart, R.E. (2006), *Radar for meteorologists*, Rineharts Publications, Nevada, USA.
- Steiner, M., R.A. Houze Jr. and S.E. Yuter (1995), Climatological characterization of three-dimensional storm structure from operational radar and rain gauge data. *Journal of Applied Meteorology*, 34, pp. 1978-2007.
- Takacs, A. , B. Brown, R. Hueftle, L. Holland, S. Madine, J. Mahoney and M. Kay (2004), *Evaluation of the oceanic cloud-top height diagnostic product: strategy of the verification methodology*, report p9.7, Research Application Program, National Center for Atmospheric Research, Boulder, CO, USA.
- Wang, J. , W.B. Rossow, Y. Zhang (1999), Cloud Vertical Structure and Its Variations from a 20-Yr Global Rawinsonde Data set, *Journal of climate*, 25, pp. 3041-3056.
- Wessels, H.R.A (1972), *Metingen van regendruppels te de Bilt*. Scientific Report WR 72-6, KNMI, de Bilt, pp. 47.
- Wessels, H.R.A. (2006), *KNMI radar methods*, Technical Report TR-293, KNMI, De Bilt.

A complete list of all KNMI -publications (1854 – present) can be found on our website

www.knmi.nl/knmi-library/knmipub_en.html



The most recent reports are available as a PDF on this site.

